Christian Ranacher, BSc

Deposition and Characterization of Proton Conductive Polymers by initiated Chemical Vapor Deposition

MASTER THESIS

For obtaining the academic degree
Diplom-Ingenieur

Master Programme of
Technical Physics

Graz University of Technology

Supervisor:
Ass. Prof. Dr. Anna Maria Coclite

Co-Supervisor
Ao.Univ.-Prof. Dipl.-Ing. Dr.techn. Roland Resel

Institute of Solid State Physics
Graz University of Technology

Graz, November 2014

To my grandfather Josef who always told me how
proud he was of me, even without words.

EIDESSTATTLICHE ERKLÄRUNG

AFFIDAVIT

Ich erkläre an Eides statt, dass ich die vorliegende Arbeit selbstständig verfasst, andere als die angegebenen Quellen/Hilfsmittel nicht benutzt, und die den benutzten Quellen wörtlich und inhaltlich entnommenen Stellen als solche kenntlich gemacht habe. Das in TUGRAZonline hochgeladene Textdokument ist mit der vorliegenden Masterarbeit/Diplomarbeit/Dissertation identisch.

I declare that I have authored this thesis independently, that I have not used other than the declared sources/resources, and that I have explicitly indicated all material which has been quoted either literally or by content from the sources used. The text document uploaded to TUGRAZonline is identical to the present master's thesis/diploma thesis/doctoral dissertation.

Datum / Date

Unterschrift / Signature

Abstract

Fuel cells are considered to be the most important energy source of the future. A major field in fuel cell research of high technological interest is the development of new and cheap electrolytes that can be successfully integrated in fuel cells as proton exchange membranes (PEM). A key feature required by such electrolytes is high proton conductivity, comparable to the actual benchmark, Nafion® ($\approx 100\,mS/cm$). High proton conductivity is obtained when a large quantity of ionizable functional groups creates ionic channels for the proton or the hydrated proton, i.e. H_3O^+, to migrate through the membrane. Electrolytes made of proton conductive polymers were synthesized using initiated Chemical Vapor Deposition (iCVD). iCVD is a solventless technique for thin film engineering and allowed to easily tune the chemical composition of the copolymer in terms of ratio between the ionic functional groups and the comonomer that ensures the stability of the copolymer in water. In a first approach, proton conductive polymers were synthesized of methacrylic acid (MAA) and 1H, 1H, 2H, 2H,-perfluorodecyl acrylate (PFDA). A detailed X-ray based investigation of the copolymers structure was performed, and out of the results, a hypothetical model for the copolymer structure was concluded. In a second approach proton conductive polymers were synthesized of methacrylic acid (MAA) and divinylbenzene (DVB). Dynamic water contact angle measurements revealed that MAA-PFDA copolymers as well as the MAA-DVB copolymers have a high chain mobility which can be beneficial for the formation of ionic channels and therefore for achieving high proton conductivities. Despite the high chain mobility of MAA-DVB copolymers, measurements with electrochemical impedance spectroscopy showed that the proton conductivity was very low. In contrast to that, MAA-PFDA copolymers achieved very promising proton conductivities as high as $55\,mS/cm$, already at room temperature. Therefore, MAA-PFDA electrolytes represent an interesting and cheap solution as proton exchange membranes for fuel cells.

Kurzfassung

Brennstoffzellen gelten als die wichtigste Energiequelle der Zukunft. Einer der Hauptbereiche in der Brennstoffzellenforschung, welcher von hohem technologischem Interesse ist, ist die Entwicklung von neuen und billigen Elektrolyten, welche als Protonenaustauschmembranen in Brennstoffzellen integriert werden können. Eine Schlüsseleigenschaft solcher Elektrolyte ist eine hohe Protonenleitfähigkeit, vergleichbar mit jener der aktuellen Benchmark, Nafion® ($\approx 100\, mS/cm$). Hohe Protonenleitfähigkeit wird erreicht, wenn eine hohe Anzahl von ionisierbaren funktionellen Gruppen ionische Kanäle erzeugt, welche dem Proton oder einem hydriertem Proton (H_3O^+) erlaubt, durch die Membran zu migrieren. Es wurden Elektrolyte aus protonenleitenden Polymeren mit initiierter chemischer Gasphasenabscheidung (initiated Chemical Vapor Deposition - iCVD) synthetisiert. iCVD ist eine lösungsfreie Methode, um Dünnfilme herzustellen und ermöglichte es, die chemische Zusammensetzung der Polymere in Bezug auf das Verhältnis zwischen den ionischen funktionellen Gruppen und dem Komonomer, welches die Stabilität der Polymere in Wasser sichert, abzustimmen. In einem ersten Ansatz wurden Elektrolyte aus methacrylic acid (MAA) und 1H, 1H, 2H, 2H,-perfluorodecyl acrylate (PFDA) hergestellt. An diesen Polymeren wurde eine detaillierte röntgenbasierte Strukturuntersuchung durchgeführt und ein hypothetisches Model für die Struktur der Polymere abgeleitet. In einem zweiten Ansatz wurden protonenleitende Polymere aus methacrylic acid (MAA) und divinylbenzene (DVB) hergestellt. Dynamische Wasserkontaktwinkelmessungen zeigten, dass die Polymerketten der MAA-PFDA als auch MAA-DVB Polymere über eine hohe Mobilität verfügen, was förderlich für die Formation von ionischen Kanälen und damit für die Protonenleitfähigkeit sein kann. Trotz der hohen Kettenmobilität der MAA-DVB Polymere zeigte elektrochemische Impedanzspektroskopie, dass die Leitfähigkeit dieser Polymere sehr gering ist. Im Gegensatz dazu erreichten MAA-PFDA Polymere bereits bei Raumtemperatur vielversprechende Protonenleitfähigkeiten von maximal $55\, mS/cm$. Damit repräsentieren Elektrolyte aus MAA-PFDA Polymeren eine interessante und günstige Lösung als Protonenaustauschmembranen für Brennstoffzellen.

Acknowledgement

First of all, I would like to thank my supervisor Anna Coclite, who has supported me throughout my thesis with patience and advice. She made it possible for me to spend two months at the famous Massachusetts Institute of Technology (MIT) to conduct the work on my thesis. I also would like to thank my co-supervisor Roland Resel for his kind support with all the X-ray experiments.

I am most grateful to Karen Gleason who invited me to the MIT. I was honoured to work in her group during my stay abroad. It was great experience to work in such famous place and to profit from their knowledge. I also would like to give special thanks to Priya Moni who introduced me to the G-lab and who was a big support during these two months.

I would like to thank Katrin Unger for her help with some of the depositions. Christian Röthel and Paul Christian are kindly acknowledged for the GIXD measurements. Furthermore I would like to thank Stephan Weinberger and Bernd Cermenek for their help with the proton conductivity measurements. Also the assistance provided by Birgit Kunert, Elisabeth Stern and Harald Kerschbaumer was greatly appreciated.

Also, I would like to thank my parents Martina and Siegfried, my sister Claudia, my grandmother Olga and my uncle Michael for supporting and helping me throughout my whole education. Last but not least I would like to give special gratitude to Bettina Webhofer, who was my major support during the five years of my studies and who always motivated me with the right words at the right time.

Contents

1 Introduction

1.1 Fuel Cells

Due to growing world wide energy consumption and concerns on the depletion of fossil energy resources, fuel cell technology has gained much attention in the last years because of high efficiency and low emissions. [1] Generally, fuel cells powered by hydrogen have a high power density and their conversion efficiency of chemical in electrical energy is relatively high. Since a fuel cell is an electrochemical power source, it is not subject to the thermodynamic Carnot limitation of heat engines. Exhausts from hydrogen fuel cells are free of air pollutants such as nitrogen oxides, carbon monoxides and residual hydrocarbons which are produced by combustion engines. Also, no carbon dioxide is produced. [2] A fuel cell is an electrochemical power source which combines the advantages of both the combustion engine and the battery. Like a combustion engine a fuel cell runs as long as fuel is provided, with no need to recharge and like a battery a fuel cell converts chemical energy directly into electrical energy. The very first fuel cell was invented in 1839 by Sir William Grove by reversing water electrolysis to generate electricity from oxygen and hydrogen using an acid electrolyte fuel cell. [3] The NASA used the first proton exchange membrane fuel cells, the 1kW Gemini power plant, as primary power source for spacecrafts of the Gemini space program in the 1960's. These fuel cells used hydrogen and oxygen as reactant gases, but they were expensive, commercially not affordable and had limited lifetimes due to the degradation of the membrane. Nevertheless, NASA was interested in future development of fuel cells because of the energy crisis in 1973. [2, 4] The second fuel cell built by General Electric powered the Biosatellite spacecraft in 1969. It used an improved membrane called Nafion® which was manufactured by Dupont. [2] Fuel cells are divided into five major categories categories, the polymer electrolyte membrane (PEM) fuel cells or PEMFC's (also known as PEFC's), solid oxide fuel cells (SOFC's), alkaline fuel cells (AFC's), phosphoric acid fuel cells (PAFC's) and molten carbonate fuel cells (MCFC's). PEMFC's are commercially most attractive because of their low operating temperatures and their high power density. These features make them a promising candidate as the next generation power sources for vehicle transportation and for applications that require clean, quiet and portable power such as powering electronic devices. PEMFC's are attractive not only because of clean exhaust emissions and high energy efficiencies, they would also provide an effective solution to the future petroleum shortage. [1–3] The current major obstacles for the commercial use of fuell cells in transport are the lack of fueling infrastructure, low performance at high temperatures (over $100°C$) and the high vehicle cost due to expensive electrode materials and in particular the electrolyte membrane. [2]

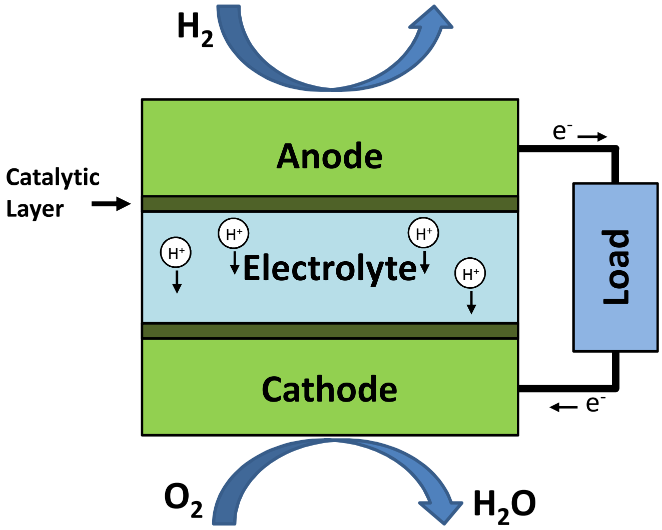

Figure 1.1: Schematic representation of a proton exchange membrane fuel cell.

Figure 1.1 shows the operating principle of a proton exchange membrane fuel cell (PEMFC). PEMFC's require humidified gases, hydrogen and oxygen (or air) as fuel for the operation. Hydrogen is decomposed into protons (H^+) and electrons (e^-) at the interface, the catalytic layer, between the anode the electrolyte. This is achieved by a catalyst which is typically platinum based. The polymer electrolyte membrane is sandwiched between the electrodes and allows protons to flow through from the anode to the cathode. Since the membrane prevents the electrons from passing through, they travel from the anode to the cathode through an external circuit, producing an electrical current and recombine at the cathode with oxygen molecules and the protons to form water. The chemical reaction is a redox reaction: [2, 3]

Anode (Oxidation): $H_2 \rightarrow 2H^+ + 2e^-$ (1.1)

Cathode (Reduction): $\frac{1}{2}O_2 + 2H^+ + 2e^- \rightarrow H_2O$ (1.2)

Overall (Redox reaction): $H_2 + \frac{1}{2}O_2 \rightarrow H_2O \quad \Delta G^\circ = -237\,\frac{kJ}{mol}$ (1.3)

The Gibbs free energy change ΔG° of the redox reaction (1.3) is related to the cell voltage via:

$$\Delta G^\circ = n\,F\,V_0 \tag{1.4}$$

With the number of electrons (n), which are involved in the overall reaction, the Faraday constant (F) and the cell voltage (V_0) at thermodynamic equilibrium under open circuit conditions. V_0 is the difference of the equilibrium electrode potentials at the cathode and the anode of the cell. It is calculated via $V_0 = -\Delta G^\circ/nF$ and is $1.23\,V$ for a single fuel cell. [3]

1.2 Proton Exchange Membranes

The use of organic cation exchange membranes as a solid electrolyte for a fuel cell was first describe by Grubb in 1959. Nowadays polymer electrolyte fuel cells are the most promising candidate for commercial use in terms of the mode of operation and applications. Polymer electrolyte membranes are usually based on proton conductive polymers. These polymers have negatively charged groups that are attached to the polymer backbone. Polymer electrolyte membranes tend to be poor proton conductors, but if water is absorbed the proton conductivity of the hydrated membranes increases dramatically and reaches values of $10 - 100\,mS/cm$. Proton conducting polymer electrolyte membranes for PEMFC's with high performance, especially for vehicle applications have to fulfil requirements such as low costs, high proton conductivities at temperatures over $100°C$ and under $0°C$, good water uptakes over $100°C$ and durabilities for 10 years and longer. To advance the commercialization of fuel cells it is crucial to develop cheap solid polymer electrolytes, that have sufficient electrochemical properties, which has become the most important area for research in PEMFC technology. [2]

1.2.1 Perfluorinated Polymer Membranes

Membranes made of perfluorinated polymers have been the subject of intense research. The key polymers which are currently used in portable fuel cell applications consist of a perfluorinated structure with attached acid groups. The mostly used perfluorinated polymer membrane is called Nafion® and is produced by DuPont. Beside that, similar membranes are produced by Asahi Glass (Flemion®), Asahi Chemical (Aciplex®-S) and Dow Chemical (Dow Membrane), which only differ in the amount of the individual monomer units. This membranes posses good thermal, chemical and mechanical properties due to their perfluorinated backbones. Figure 1.2 shows the chemical structure of these perfluorinated electrolyte membranes. Because of its high proton conductivity ($\approx 100\,mS/cm$), good chemical stability and mechanical strength, Nafion® is considered to be the most suitable polymer membrane for commercial use. [2, 5] Since Nafion® was developed in 1968 by DuPont, the performance of PEMFC's has improved significantly and lifetimes of over 50000 hours were achieved with the commercial Nafion®120. Various types of Nafion® are available, which differ in molecular weight and thickness, respectively. For example, in dry state Nafion®120 has an equivalent weight of 1200 and a thickness of $260\,\mu m$, while Nafion®117 has molecular weight of 1100 and a thickness of $175\,\mu m$. [2]

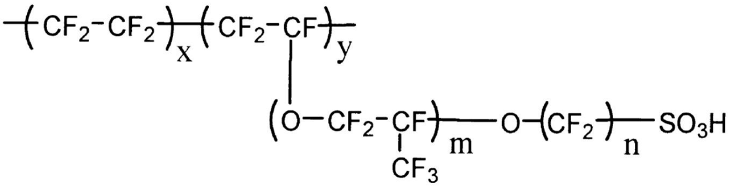

Nafion®117	$m \geqq 1$, $n=2$, $x=5\text{-}13.5$, $y=1000$
Flemion®	$m=0, 1$; $n=1\text{-}5$
Aciplex®	$m=0, 3$; $n=2\text{-}5$, $x=1.5\text{-}14$
Dow membrane	$m=0$, $n=2$, $x=3.6\text{-}10$

Figure 1.2: Chemical structures of perfluorinated polymer electrolyte membranes. Reprinted from [2]

In general, limiting factors for the commercialization of this membranes are insufficient ionic conductivities at low humidities and temperatures above $100°C$, chemical degradation at high temperatures and the high costs of perfluorinated polymers. These factors can have a negative influence on the fuel cell's performance and therefore limit the operation conditions for fuel cells. The proton conductivity of Nafion® is $\approx 100\, mS/cm$ when it is fully hydrated, but the conductivity decreases dramatically at operation temperatures above the boiling point of water because amount of absorbed water in the membrane decreases. [2] While the proton transport in Nafion® with different operation parameters, such as temperature, membrane thickness and water content, have been analysed, the transport phenomena is yet not fully understood. Beside the transport phenomena and the structure analysis of Nafion® another research field of interest is to improve the performance of Nafion® by making modifications to the membrane and in general to find a suitable alternative to Nafion® which has similar chemical and mechanical properties. [5]

Structure of Nafion®

As already mentioned, Nafion® is widely used in PEMFC's due to its high proton conductivity. Nafion is synthesized by copolymerization of variable amount of unsaturated perfluoralkyl sulfonyl fluoride with tetrafluoroethylene. It is available with various amounts of sulfonic acid groups which acts as proton conductor. Investigations with small-angle X-ray scattering (SAXS) as well as with X-ray diffraction (XRD) showed the presence of a crystalline matrix in the Nafion® structure, which has been attributed to the hydrophobic PTFE chains. In the hydrated form Bragg peaks were observed that correspond to a spacing of $3 - 5\, nm$, which is characteristic for systems that contains ionic clusters within a crystalline matrix. The term ionic cluster refers to nano-phase separated, hydrated ionic groups. Based on further structure investigation by SAXS and XRD, a model was concluded. This model describes the morphology of hydrated Nafion® with ionic clusters of sulfonate-ended perfluoroylkyl ether groups that have approximately the shape of a sphere with a diameter of $\approx 4\, nm$ and are organized as inverted micelles. Since it is required to have a percolation pathway in the membrane, it was further proposed that this ionic clusters are interconnected by narrow channels that have a width of $\approx 1\, nm$. This channels with $-SO_3^-$ groups allow the proton transport between the clusters via hopping from one group to another. The proposed model is known as the cluster-network model and is shown in figure 1.3. It describes the morphology for hydrated Nafion® with different phases. A semicrystalline fluorocarbon phase with the hydrophobic PTFE backbone, which ensures the stability in water, an interfacial region that contains the sulphonate groups and the ionic clusters which contains the absorbed water.

The cluster-network model explains the proton transport properties of Nafion® and has received significant acceptance in literature, but also other models have been proposed to describe the morphology more accurately. [3, 6, 7]

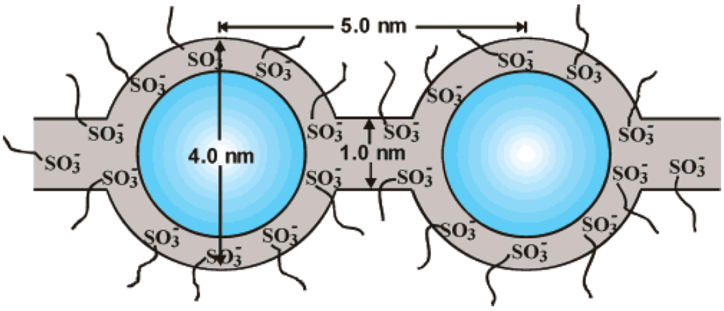

Figure 1.3: Cluster-network model for hydrated Nafion®. Reprinted from [7]

1.2.2 Hydrocarbon Polymer Membranes

Perfluorinated membranes suffer from significant drawbacks for large scale commercialization, which include the high costs and use of fluorine-based chemistry. Therefore recent effort has been directed to synthesize and study non-perfluorinated polymer membranes, which are commonly referred as hydrocarbon membranes. [8] For commercial use it is required to develop cheaper materials, that can provide the required electrochemical properties and if this can be done one could even make a compromise in terms of lifetime and the mechanical properties of the membrane. In the early days of fuel cell development the use of hydrocarbon polymer electrolytes was rejected due to their low thermal and chemical stability. However, since the required lifetime for vehicle transport or for powering electronic devices is significant shorter than for spacecrafts, hydrocarbon polymers could establish. [2] The use of hydrocarbon polymers provides some advantages over perfluorinated polymers:

1. They are less expensive than perfluorinated ionomers.
2. They permit the introduction of pendant polar groups, to improve the water uptake. The absorption of water is restricted to this groups.
3. By ingenious molecular design the decomposition of hydrocarbon polymers can be prevented.
4. Hydrocarbon polymers can be recycled by conventional methods. [2, 5]

Since catalyst and fuel cell assembly technologies have improved, which also brought benefits to the lifetimes of the related materials, hydrocarbon polymers have become a very promising building block to high performance polymer electrolyte membranes. [2]

2 Fundamentals

2.1 Polymers

The term polymer means "many parts" and designates a large molecule which is made up of smaller repeat units, that are covalently bonded together and have a huge diversity in terms of chemistry and structure. They are mainly carbon based, but there exist also silicon, sulfur, or nitrogen based polymers. Polymers have in general a high molecular weight around $5000\,amu$, which means that their weight is 5000 times higher then a twelfth of the weight of a carbon atom. Polymers that have only a low molecular weight and a small number of repeat units respectively, are called **oligomers**. A polymer is formed by the combination of **monomer** units from the same or different species. The **repeat unit** is the portion of which the polymer can be synthesized by linking a large amount this repeat units together. Repeat units can exist of one monomer molecule or of a composition of different monomer units. This definition has some limitations because due to the architecture of polymers it is not always possible to define a repeat unit. Figure 2.1 shows the repeat units of polyethylene and polystyrene, which are widely in packaging for plastic bags, bottles, etc. [9]

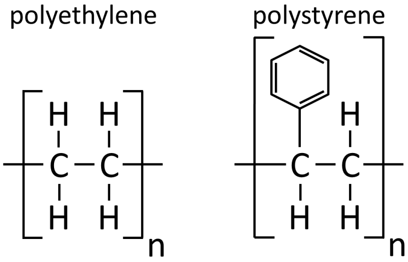

Figure 2.1: Repeat unit of polyethylene and polystyrene

The **degree of polymerization** (DP) describes the number of repeating units in a polymer molecule. It is evident that this definition is only useful for polymers with regular identifiable repeating units. The degree of polymerization is related to the molecular weight (M) of the polymer via $M = (DP)M_0$, where M_0 is the formula weight of the repeating unit. The end groups of a polymer chain differ from the repeat units and are usually not known. Since a polymer consists of thousands of repeat units compared to two end groups each, their effect on the properties can be neglected and a polymer is only described in terms of their repeat units. The **functionality** of a monomer describes the number of sites that are available for bonding to other monomer units in a polymerization reaction. While a **homopolymer** consists of only one monomer species, a **copolymer** contains two or more precursor species. The most important classes of copolymers are shown in Figure 2.2. [9]

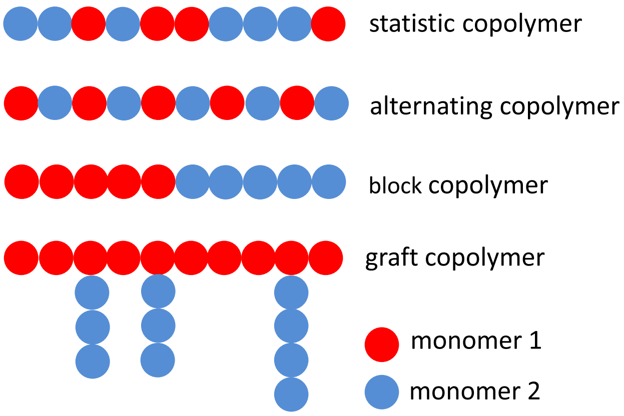

Figure 2.2: Schematic representation of copolymer classes.

In alternating copolymers each monomer species is joined by the other monomer species. A statistical copolymers contains alternating parts as well as "random copolymer" parts in which the probability to find a monomer species on a given site depends only on its relative proportion in the reaction mixture. Block copolymers have parts with containing only one species followed by parts which contains the other monomer species. So called graft copolymers are formed by growing polymer branches of one species on another polymer. [9]

Step-Growth Polymerization and Chain-Growth Polymerization

Most polymerization reactions can be classified either as step-growth polymerizations or chain-growth polymerizations. In step-growth polymerization reactions any two monomers that are present in the reaction mixture can combine at any time and the growth process is not confined to certain activated sites, where chains are already forming. This means that the monomers in the reaction feed are used quickly and the average molar mass of the polymers growths with time. In chain-growth polymerization reactions an activated monomer reacts with another monomer in the reaction mixture and the resulting unit attacks another monomer unit and so on. The monomer in the feed is used slowly since the reaction is confined to certain growing chains. This leads to molecules with a high average molecular mass and a long reaction time just increases the yield. [10]

2.1.1 Free Radical Polymerization

Free radical polymerization process is a chain growth polymerization and it is widely used for synthesizing polymers. [9] A big advantage over step-growth polymerization is that it is much faster. The functionality of the monomer species must be two or higher in order to produce polymers from its reactions. This functionality can be achieved either by opening a double bond or a ring, or by co-reactive functional groups. Free radical polymerization consists of three major steps. The initiation, propagation and termination step. For comparison, in a step growth polymerization is only one step present.

Initiation

During the initiation step free radicals are produced and introduced in the system to start the reaction. A free radical is an atom, molecule or ion with unpaired valence electrons or an open electron shell and is therefore highly reactive. The production of this radicals can be accomplished by different methods and the most common way is to thermally decompose a so called initiator (I) which decomposes into two free radicals, the so called primary radicals ($R^{\bullet}$):

$$I \xrightarrow{\mathrm{k_d}} 2R^{\bullet} \tag{2.1}$$

The rate constant for this reaction is k_d, which is temperature dependent. Also the reaction of a radical ($R^{\bullet}$) with a monomer (M) is an initiation reaction:

$$R^{\bullet} + M \xrightarrow{\mathrm{k_I}} M_1^{\bullet} \tag{2.2}$$

The result of the this reaction is an activated monomer, which is a radical-ended monomer unit.

Propagation

A propagation step in a chain reaction is defined as a reaction in which products are formed and the site of the reactive center changes, but the number of active centers stays constant. The general equation for a propagation step is:

$$M_m^{\bullet} + M_n \xrightarrow{\mathrm{k_P}} M_{m+n}^{\bullet} \tag{2.3}$$

Where $M_m^{\bullet}$ is surface radical with the length m and M_n is a polymer with the length n. The result of this reaction is an activated polymer with the length $n + m$.

Termination

Termination is a reaction where two radicals are annihilated. This can either be a reaction between two primary radicals, a primary radical with an activated monomer/polymer or a reaction between two activated monomers/polymers:

$$R^{\bullet} + R^{\bullet} \xrightarrow{\mathrm{k_T}} 2R \tag{2.4}$$

$$R^{\bullet} + M_m^{\bullet} \xrightarrow{\mathrm{k_{T'}}} M_m \tag{2.5}$$

$$M_m^{\bullet} + M_n^{\bullet} \xrightarrow{\mathrm{k_{T''}}} M_{m+n} \tag{2.6}$$

The termination reactions end the polymerization process and the result is a so called dead polymer which is stable and not reactive.

2.1.2 Copolymerization

Copolymerization of two or more monomer species is a widely used way to modify the balance of properties of polymers. [9] As already described in chapter 1.2.1, Nafion® consists of hydrophobic and hydrophilic acid parts, which together as a copolymer give both, good proton conductivity and stability in water. The composition of the copolymers, that are synthesized by free-radical copolymerization, depends on the monomer ratio at the surface. This fraction on the surface differs from the monomer composition in the feed, if the monomer species have different volatility (e.g., if they have different saturation pressures). Additionally the fraction of the monomer species depends on their reactivity ratios r_i. In a copolymerization of generic monomers, M_1 and M_2 that add to a copolymer chain that terminates with M_1, the reactivity ratio r_1 can be defined as the ratio between the reactions constants k_{11} and k_{12}, according to the following possible reactions: [11]

$$copol - M_1^{\bullet} + M_1 \xrightarrow{\mathrm{k}_{11}} copol - M_1 - M_1^{\bullet} \tag{2.7}$$

$$copol - M_1^{\bullet} + M_2 \xrightarrow{\mathrm{k}_{12}} copol - M_1 - M_2^{\bullet} \tag{2.8}$$

Analogously, one can identify the reactivity ratio r_2 for a growing copolymer chain terminating with the monomer unit M_2. The reactivity ratios account for the probability of the propagating species to add to the same or the other species, which determines the final copolymer structure. [11] The reactivity of the monomer species cannot be easily predicted from their behaviour in a homopolymerization, but can be described by a simple copolymer model. This model accounts for the behaviour of many important systems which allows statistical estimation of the polymer composition and the monomer sequence in the copolymer from little data. [9] The simple copolymer model leads for low conversions of monomers to the Finemann-Ross equation which allows to predict the chemical composition of a copolymer:

$$\frac{f}{F}(F-1) = r_1 \frac{f^2}{F} - r_2 \tag{2.9}$$

With f the monomer fraction adsorbed on the surface F the monomer fraction in the copolymer. [12]

2.1.3 Polymer Crystals

Besides amorphous structures, polymers can also aggregate in a state that is between a crystalline solid and an amorphous liquid, which is referred as liquid crystal. Polymers in this state are highly anisotropic in some of its properties. To be able to aggregate in this state a molecule must be geometrically anisotropic, usually long and narrow. Liquid crystals can be classified into three major types, **nematic**, **cholesteric** and **smectic** liquid crystals. Figure 2.3 shows a schematic representation of an isotropic liquid, a nematic and a smectic liquid crystal and of a solid crystal.

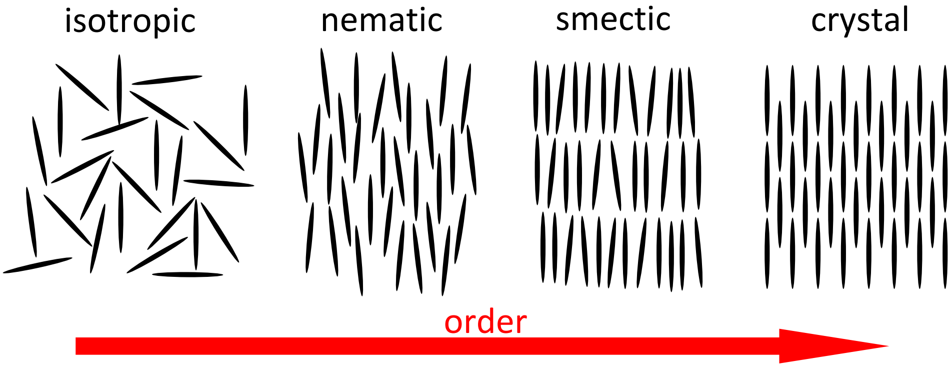

Figure 2.3: Schematic representation of different structural orders.

The molecules in a nematic liquid crystals have a high degree of long range orientational order, which means that the molecules have a preferred orientation with their long axes approximately parallel, but no long range transitional order. The cholesteric phase is also a nematic phase with a screw axis superimposed to the preferred orientation, which leads to a helical structure. Smectic liquid crystals have beside the orientation also a layered structures, with various possible molecular arrangements. In a smectic A and smectic C liquid crystals, molecules are upright or tilted, respectively in each layer, but have no positional order within the layer. In a smectic B liquid crystal, the molecules are upright in each layer as in smectic A but the molecular centres in each layer are hexagonal close packed. The layer thickness in smectic phases is usually close to the full length of the molecules. [13] Polymers can arrange into liquid crystals either by connecting the LC forming units head-to-tail, which results in a main-chain LC or by attaching this units as side-chain to the main polymer backbone (see figure 2.4). [14]

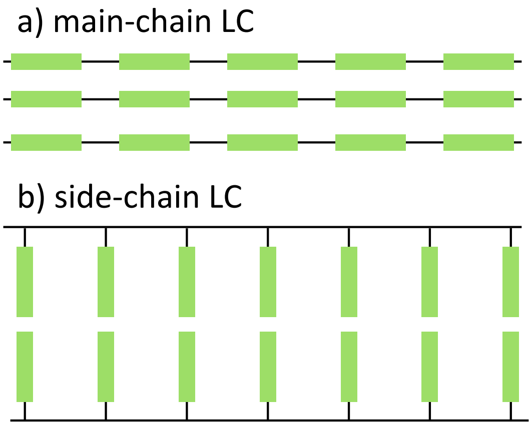

Figure 2.4: Schematic representation of a main-chain (a) and side-chain (b) liquid crystal.

2.2 Proton Transport in Polymers

The investigation of proton conduction in solids started when it was discovered that ice can conduct electricity and the research expanded to proton conducting polymer electrolytes for applications such as proton exchange membranes in fuel cells. While typical electrical conductors like metals can not conduct ions or protons, since this ions are fixed in the crystal lattice, proton conductivity can be found in various materials, from rigid inorganic oxides at high temperatures to organic polymers at room temperature. The proton transport in polymers is based on three different mechanisms, which are shown in figure 2.5. This mechanisms are the Grotthuss or hopping mechanism (a), the vehicle or diffusion mechanism (b) and the direct transport of protons via polymer chain segmental motions (c).

Hopping transport - Grotthuss mechanism

In the Grotthuss mechanism the mobility of the protons depends on the rate of formation and cleavage of hydrogen bonds between a hydrated proton, a so called hydronium (H_3O^+), and a water molecule. The protons are transported by hopping from one hydrolized ionic site to another. It is characterized by a high proton mobility which leads to high proton conductivities.

Vehicle or diffusion mechanism

In the vehicle mechanism, a proton combines with a solvent molecule, e.g. H_2O to form a hydronium and diffuses due to a gradient in the proton concentration. This

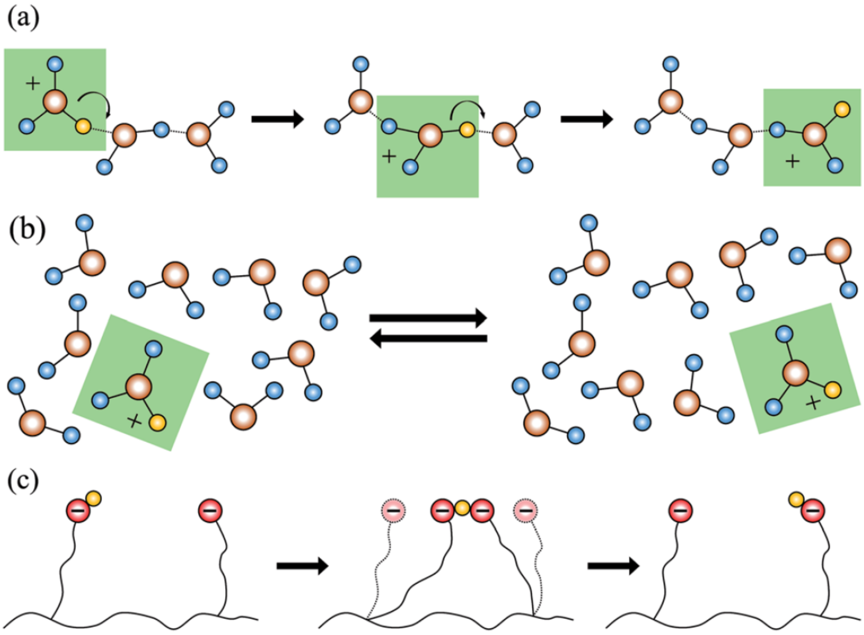

Figure 2.5: Proton transport mechanisms in polymers. a) Grotthuss or hopping mechanism b) Vehicle or diffusion mechanism c) Direct transport via polymer chain motions. Reprinted from [15]

transport mechanism is much slower than the hopping transport. It is characterized by a lower proton mobility which leads to a lower proton conductivity.

Direct transport

Protons can also be transported via segmental motions of polymer chains. This transport mechanism is restricted to polymers in the amorphous phase where the polymer chains can easily move.

At constant temperature and high relative humidity (RH), protons are transported via the Grotthuss mechanism and via the vehicle mechanism at low RH. By increasing the temperature the vehicle mechanism increasingly dominates, as hydrogen bonds get elongated and start to cleave. Therefore the dominant transport mechanism and the proton conductivity depends on the temperature as well as on the RH. In general, the proton conductivity increases with temperature to a certain extent and with the RH. [15–17]

2.3 Principle of X-Ray Diffraction

Diffraction effects occur when electromagnetic radiation strikes periodic structures with geometrical length scales close to scale of the wavelength of the radiation. In the relevant energy range for X-ray diffraction three different types of interaction between the radiation and matter can occur. Two types of inelastic scattering, the so called photoionization and Compton scattering, where energy from the radiation is transferred to an electron and the, for X-ray diffraction investigations important elastic scattering, also known as Thomson scattering. In the latter scattering effect, electrons get excited by the incoming radiation and oscillate like a Hertz dipole at the frequency of the incoming electromagnetic radiation and therefore become a source of dipole radiation. The energy and thus the wavelength λ of the radiation is conserved for Thomson scattering, which is in contrast to the two inelastic processes. If the time dependence is neglected, an electromagnetic plane wave is described via $\mathbf{E}_0\, exp(-i\,\mathbf{k}\,\mathbf{R})$ where $\mathbf{E}_0$ is the electric field vector, $\mathbf{k}$ the wavevector and $\mathbf{R}$ the position. The wave vector $\mathbf{k}$ describes the direction of the radiation. It has the dimension of an inverse length and is related to the wavelength via $\mid \mathbf{k} \mid = 2\pi/\lambda$. If monochromatic and parallel electromagnetic radiation is scattered on a whole group of atoms that are periodically arranged on a crystal lattice, it can be derived that the scattered intensity of the radiation is:

$$I(\mathbf{R}) = \mathbf{E}_0\, \frac{Z\, r_e}{|\mathbf{R}|}\, C\, exp\,(-i\,\mathbf{k'}\,\mathbf{R}) \sum_{n_1 n_2 n_3} exp\,(-i\,(\mathbf{k'} - \mathbf{k})\,\mathbf{r}_{n_1 n_2 n_3}) \tag{2.10}$$

With Z the number of electrons of the atom, C the polarization factor, $\mathbf{k}$ the incoming wavevector, $\mathbf{k'}$ the scattered wavevector and $\mathbf{r}_{n_1,n_2,n_3}$ the lattice vector. The lattice vector describes the positions of the atoms on the crystal lattice via:

$$\mathbf{r}_{n_1 n_2 n_3} = n_1\, a\, \mathbf{c}_1 + n_2\, a\, \mathbf{c}_2 + n_3\, a\, \mathbf{c}_3 \tag{2.11}$$

If we assume a simple cubic lattice, n_i are integer numbers to assign one specific atom in the lattice, a is the interatomic distance and $\mathbf{c}_i$ are the unit vectors of the crystal coordinate system. The difference between the incoming and scattered wavevector ($\mathbf{k'} - \mathbf{k}$) in (2.10) is recognized as the important scattering vector $\mathbf{q}$ and can be calculated via:

$$\mathbf{q} = \mathbf{k'} - \mathbf{k} \tag{2.12}$$

If an electromagnetic wave is scattered on a crystal lattice, and the angle of the incoming wave equals the angle of the scattered wave (see figure 2.6), it can be derived from geometrical considerations that the magnitude of the scattering vector is:

$$|\mathbf{q}| = 4\pi sin(\theta)/\lambda \tag{2.13}$$

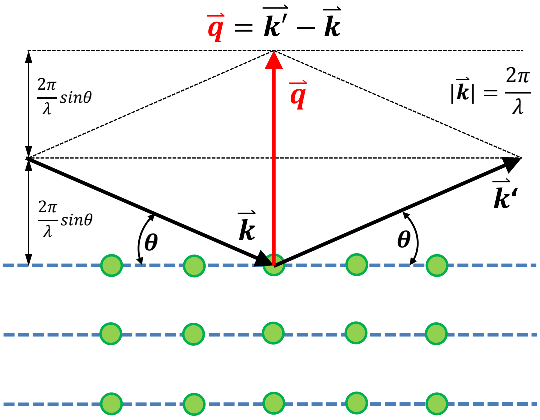

Figure 2.6: Geometry of the scattering vector.

By expanding the summation factor in (2.10) into the three individual terms and using the geometry of the simple cubic lattice, it can be found that the field amplitude of the scattered beam is proportional to:

$$\sum_{n_1=0}^{N_1-1} \sum_{n_2=0}^{N_2-1} \sum_{n_3=0}^{N_3-1} exp\left(-i\,\mathbf{q}\left[n_1\,a\,\mathbf{c}_1 + n_2\,a\,\mathbf{c}_2 + n_3\,a\,\mathbf{c}_3\right]\right) \tag{2.14}$$

Where the scattering vector **q** is already substituted for **k’** − **k**. This expression can be converted into the so called interference function $\Im$(**q**) by evaluating each of the three terms by the formula of the geometric sum and multiplying by the complex conjugate:

$$\Im\left(\mathbf{q}\right) = \frac{sin^2\left(N_1\,a\,\mathbf{q}\,\mathbf{c}_1/2\right)}{sin^2\left(a\,\mathbf{q}\,\mathbf{c}_1/2\right)} \cdot \frac{sin^2\left(N_2\,a\,\mathbf{q}\,\mathbf{c}_2/2\right)}{sin^2\left(a\,\mathbf{q}\,\mathbf{c}_2/2\right)} \cdot \frac{sin^2\left(N_3\,a\,\mathbf{q}\,\mathbf{c}_3/2\right)}{sin^2\left(a\,\mathbf{q}\,\mathbf{c}_3/2\right)} \tag{2.15}$$

The interference function describes the distribution of scattered intensity in the space around the crystallite. If N_1, N_2 and N_3 is large, the three factors in the interference function only differ from zero if the arguments of sin^2 of the denominator become multiple integers (h,k,l) of π. This leads to the following condition for highest value of the interference function:

$$\Im(\mathbf{q}) \to max \Leftrightarrow \begin{aligned} a\,\mathbf{q}\,\mathbf{c}_1 &= 2\pi h \\ a\,\mathbf{q}\,\mathbf{c}_1 &= 2\pi k \\ a\,\mathbf{q}\,\mathbf{c}_1 &= 2\pi l \end{aligned} \tag{2.16}$$

This set of equations are the Laue conditions for the special case of a simple cubic lattice. They describe the relation between the lattice vectors and the scattering vector at the position of constructive interference. The magnitude of **q** at $I\left(\mathbf{r}\right) \to max$ can be obtained from this set of equations by dividing by a and adding the up the squares of three equations. This leads to $|\mathbf{q}|$ after calculating the product of **q** and the vectors of the coordinate system $\mathbf{c}_i$. Finally dividing by 2π and taking the square root leads to the condition for maximum intensity:

$$I\left(\mathbf{r}\right) \to max \Leftrightarrow \frac{|\mathbf{q}|}{2\pi} = \frac{\sqrt{h^2+k^2+l^2}}{a} \tag{2.17}$$

Which can be rewritten by substituting the magnitude of the scattering vector:

$$I\left(\mathbf{r}\right) \to max \Leftrightarrow 2\,\frac{a}{\sqrt{h^2+k^2+l^2}}\,sin\theta = \lambda \tag{2.18}$$

The integer triple hkl are the so called Miller indices which describe any set of planes in the crystal lattice. The distance between two particular planes is found by a geometric consideration that this interplanar spacing depends on the unit cell parameter a and the Miller indices, which leads to:

$$d_{hkl} = \frac{a}{\sqrt{h^2+k^2+l^2}} \tag{2.19}$$

From (2.17) and (2.19) an important relation between the scattering vector and the interplanar distance can be obtained:

$$|\mathbf{q}| = \frac{2\pi}{d_{hkl}} \tag{2.20}$$

Substituting (2.19) in (2.18) leads to the famous Bragg equation:

$$2\,d_{hkl}\,sin\theta = \lambda \tag{2.21}$$

The Bragg equation describes the position of X-ray scattering peaks and the peak positions are called Bragg reflections. It relates the scattering angle θ to the lattice plane distances d_{hkl}. If the scattered intensity is measured in a X-ray experiment, the detected intensity peaks can be assigned to lattice plane distances and therefore the crystal structure can be concluded. The Laue conditions and the Bragg condition are equivalent. They were derived for a simple cubic lattice but they can be generalized and are valid for any crystal lattice. Besides from the Laue conditions, the Bragg equation can also be derived geometrically from figure 2.7.

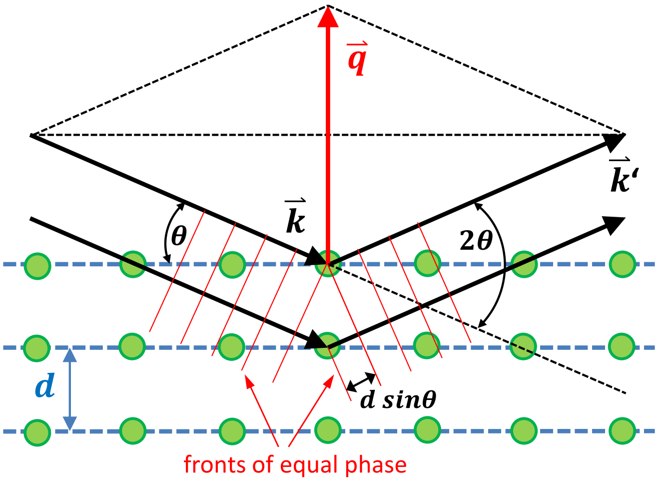

Figure 2.7: Visualization of the Bragg equation

If an incident X-ray wave hits a lattice plane under a certain angle θ, the beam is diffracted by the planes whereby the beam which is diffracted from lower planes has a longer path. To get constructive interference, the length of this path has to be a multiple integer of λ. From simple geometrical considerations it can be obtained that this path difference is $2d\,sin\theta$, which leads to the more popular form of the Bragg equation:

$$n\,\lambda \;=\; 2d\,sin\theta \tag{2.22}$$

Where n is the order of the reflection. Since usually 3D crystals are investigated, which act as diffraction gratings, the Bragg equation in the form (2.21) is preferred. [18]

3 Methods

The aim of this section is to give a short explanation of the methods that were used to synthesize and characterize the polymer films. A more detailed explanation can be found in the references.

3.1 initiated Chemical Vapor Deposition

Polymer films and coatings can be synthesized in a number of ways. The most common ways are solution-based, where polymer solutions or emulsions are applied to the surface by spraying, dipping or coating with subsequently evaporation of the solvent. [19] The use of solvent based techniques has some limits in terms of substrates (e.g. if the solvent dissolves the substrate) and if it is required to use precursors with very different solubilites. Therefore it is crucial to develop solventless dry methods for engineering films. The most common used dry method to form polymer films is plasma-enhanced chemical vapor deposition (PECVD). [20] Due to extensive crosslinking, the obtained polymer compositions from PECVD can deviate significantly from a linear polymer stoichiometry.

It has been demonstrated that initiated chemical vapor deposition (iCVD) is a solvent free method which allows to produce addition polymers identical to those produced from solution-based polymerization processes. [19] With iCVD it is possible to conformally coat planar as well as complex three-dimensional structures in a single step polymerization, while having control over the thickness of the coating in nanometer scale. [19]

iCVD is a free-radical polymerization method. The initiator and the monomer species are delivered in the gas phase into a vacuum chamber in which the pressure is typically maintained in the range between $0.1 - 1\,Torr$. The initiator species always contains a labile bond (e.g. $O - O$ bond in peroxides) which can be decomposed by thermal activation. To create these initiator radicals out of the initiator vapor, a heated filament array, which is typically heated between $200°C$ and $400°C$, is used. [11, 19] Figure 3.1 shows a schematic representation of an iCVD reactor. The stage on which the sample is placed is maintained at temperatures usually lower than $50°C$ to promote the adsorption of the monomer species on the surface. Due to this low substrate temperature and the fact that iCVD is solventless, practically every substrate can be coated with this technique. The top of an iCVD reactor is usually made of a transparent glass window which allows the in-situ monitoring of the film growth.

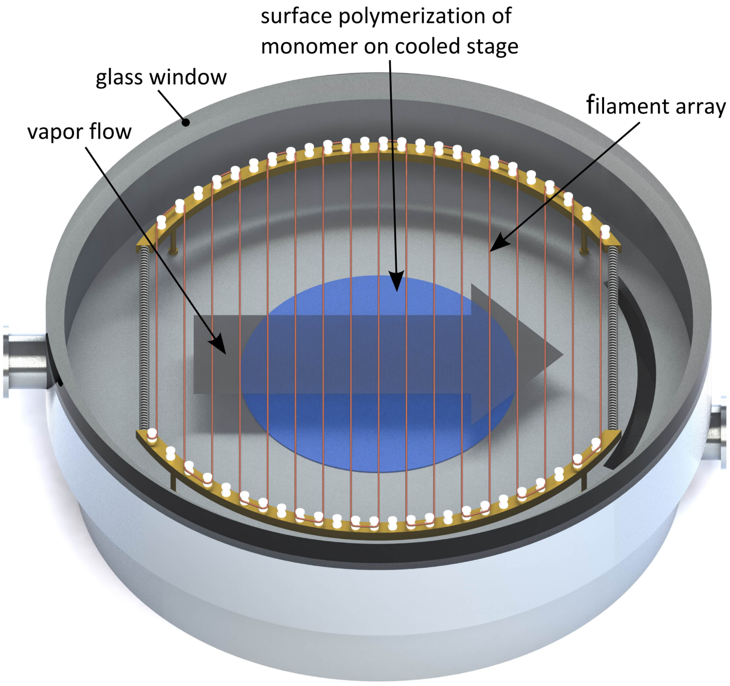

Figure 3.1: Schematic representation of an iCVD reactor setup.

The chemical process behind the iCVD polymerization is a free radical polymerization. But since this technique also involves the transport and adsorption of the radicals and monomers to and onto the polymerization site, the proposed reaction mechanism slightly differs from the conventional free radical polymerization which was described in section 2.1.1. The proposed mechanisms for the iCVD polymerization are shown in figure 3.2 and described in detail with the equations (3.1)-(3.8). The reaction mechanisms are divided into gas phase reactions, gas to surface processes and the surface reactions. In gas phase reactions, the initiator is thermally decomposed (1) in the vicinity of the heated filaments. The gas to surface processes are the diffusion and adsorption (2) of the monomer species and the primary radicals from the vapor phase onto the substrate surface. The surface reactions are the actual polymerization reactions (3) in which propagation and termination events occur to form polymer chains. In a propagation event a primary radical or a polymer radical reacts with another monomer unit to extend the polymer chain. Termination is the reaction between two radical species and thus ends the polymerization process. [19, 21]

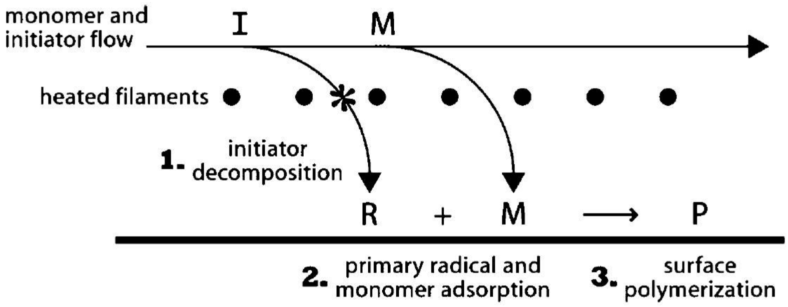

Figure 3.2: Reaction mechanism proposed for the iCVD polymerization. Reprinted from [19]

Gas phase reactions

initiator decomposition:

$$I_{(g)} \xrightarrow{\mathrm{k_D}} 2R^{\bullet}_{(g)} \tag{3.1}$$

Gas to surface processes

primary radical adsorption:

$$R^{\bullet}_{(g)} \xrightarrow{\mathrm{k_{ad,R}}} R^{\bullet}_{(ad)} \tag{3.2}$$

monomer adsorption:

$$M_{(g)} \xrightarrow{\mathrm{k_{ad,M}}} M_{(ad)} \tag{3.3}$$

Surface reactions

Initiation:

$$R^{\bullet}(ad) + M(ad) \xrightarrow{\mathrm{k_I}} M_1^{\bullet}(ad) \tag{3.4}$$

Propagation:

$$M_m^{\bullet}(ad) + M(ad) \xrightarrow{\mathrm{k_P}} M_{m+1}^{\bullet}(ad) \tag{3.5}$$

Termination:

$$M_m^{\bullet}(ad) + M_n^{\bullet}(ad) \xrightarrow{\mathrm{k_T}} M_{m+n}(ad) \text{ and } M_m(ad) + M_n(ad) \tag{3.6}$$

Primary radical termination:

$$M_m^{\bullet}(ad) + R^{\bullet}(ad) \xrightarrow{\mathrm{k'_T}} M_m(ad) \tag{3.7}$$

Primary radical recombination:

$$R^{\bullet}(ad) + R^{\bullet}(ad) \xrightarrow{\mathrm{k''_T}} R_1(ad) \tag{3.8}$$

In iCVD the substrate temperature, the monomer flow rate, and the filament temperature all impact the deposition kinetics, but the dominant parameter is in most cases the ratio between the monomer partial pressure (P_M) and the saturation pressure at the substrate temperature (P_{sat}). [11] The ratio P_M/P_{sat} is directly related to the amount of monomer which is adsorbed onto the surface of the substrate. Maintaining the substrate temperature low promotes the adsorption of the monomer, which leads to a high rate of polymerization and therefore to high deposition rates and polymer chains with high molecular weight. Most film growth iCVD processes are carried out at P_M/P_{sat} values of 0.3 to 0.7. Operating within this range concentrates monomer species to liquid-like concentrations on the substrate surface and promotes uniform film growth without leading to undesirable liquid-phase condensation $(P_M/P_{sat} \approx 1)$. [22]

It was reported in literature that the copolymerization kinetics is strongly dependent on the fraction f of each monomer, which is adsorbed on the surface. [11] The amount of each monomer adsorbed on the surface can be quantified through the ratio between the monomer partial pressure (P_M) and the saturated vapor pressure (P_{sat}) at the substrate temperature. Therefore, for a copolymer which consists of the species M_1 and M_2, the fraction of species M_1 adsorbed on the surface f_{M_1} can be calculated via:

$$f_{M_1} = \frac{\left(\frac{P_M}{P_{sat}}\right)_{M_1}}{\left(\frac{P_M}{P_{sat}}\right)_{M_1} + \left(\frac{P_M}{P_{sat}}\right)_{M_2}} \times 100 \tag{3.9}$$

The fraction of M_1 adsorbed on the surface is correlated to the actual concentration of M_1 in the copolymer.

3.2 Fourier Transform Infrared Spectroscopy

Fourier transform infrared spectroscopy is a method to study and identify the chemical composition of a sample by measuring the absorbance of electromagnetic infrared radiation in dependence of the wavelength. The used wavelength range lies typically between $2.5\,\mu m$ and $25\,\mu m$ which corresponds to wavenumbers between $4000\,cm^{-1}$ and $400\,cm^{-1}$. The resonance frequencies of the rotational and vibrational modes of chemical bonds (e.g. symmetric and asymmetric stretching of the H-O bonds in a water molecule) are in this range and therefore the radiation is absorbed and excites this modes. The chemical composition of the investigated sample can be determined by analysing the absorption spectra and assigning the absorptions to certain bonds of molecules.

The most straightforward approach to perform this measurement would be to shine a monochromatic light beam on the sample, vary the wavelength in the desired range and record the outcoming intensity of the radiation. Fourier transform infrared spectroscopy uses a more practicable approach, by shining a light beam on the sample which contains many frequencies and measuring how much this beam is absorbed by the sample. This is repeated many times with different combinations of frequencies to cover desired range of wavelengths with the desired resolution. This combinations of frequencies are achieved by shining broadband radiation into a Michelson interferometer, which is a configuration of mirrors. One of the mirrors is moved, resulting in a periodically blocking and transmitting of certain wavelengths due to interference effects. Each wavelength is modulated at certain rates which this leads to the continuously changing spectrum on the output of the interferometer. The result of this measurement is a so called interferogram which needs to be processed by a Fourier transformation to get the absorption at each wavelength, hence the so called infrared spectra. Table 3.1 summarizes some characteristic absorptions. [23, 24]

Table 3.1: Characteristic IR absorptions

wavenumber $[cm^{-1}]$	bond	functional group
$3500 - 3000$	$O - H$ stretch	carboxylics acids ($COOH$) or H_2O
$3000 - 2750$	$C - H$ stretch	CH_2 and CH_3
$1760 - 1690$	$C = O$ stretch	carboxylic acids ($COOH$) and acrylates ($COOR$)
$1500 - 1400$	$C - C$ stretch (in-ring)	aromatics
$1250 - 1200$	$C - F$ stretch	CF_2
1150	$C - F$ stretch	$CF_2 - CF_3$

3.3 X-Ray Crystallography

X-ray crystallography provides various techniques that are widely used to determine the atomic and molecular structure of atomic or molecular crystals. The basic principle of these methods is to measure the angles and intensity of X-rays, that are diffracted by the crystalline samples. From this measurements various information besides the crystal structure can be gained.

3.3.1 X-Ray Diffraction

X-ray diffraction (XRD) is a widely used technique for investigating the structure of thin films and measuring Bragg reflections with a so called $\theta/2\theta$ diffractometer. In order to derive microstructural information of the Bragg reflections, their position, their intensity and their shape is of interest. As described in in section 2.3 the interplanar distance of a crystal can be determined from the angular position of the Bragg peaks. Since the scattered intensity depends on the distance of the sample to the detector, the setup is configured in a way that the detector moves in a hemisphere, keeping the distance to the sample constant. During the measurement the source and the detector are moved on this hemisphere equally to keep the angle of the incident beam and the outgoing beam constant $\theta_{in} = \theta_{out}$, which is the so called specular condition. This measurement can also be understood as a variation of the outgoing beam with respect to the incoming beam and this angle is always 2θ, which leads to the name "$\theta/2\theta$ scan" for this measurement. Figure 3.3 show a schematic representation of a $\theta/2\theta$ diffractometer. Such a diffractometer consists of a X-ray source, a Beta-filter as monochromator, various slits to adjust the beam shape, the sample stage and the detector. [18]

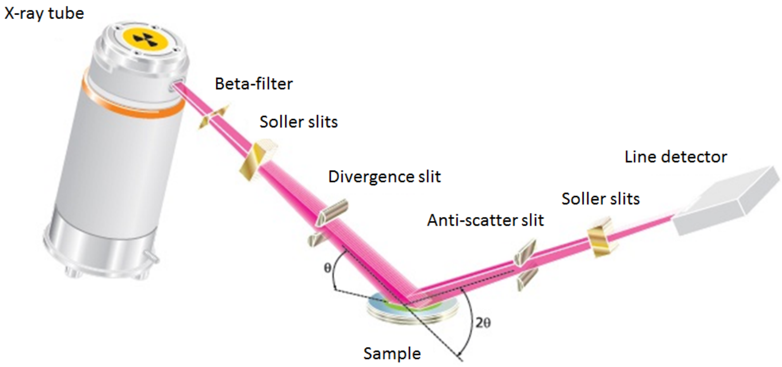

Figure 3.3: Schematic representation of $\theta/2\theta$ diffractometer. Reprinted from [25]

Since $\theta_{in} = \theta_{out}$, the scattering vector **q** is always parallel to the normal vector of the substrate and has therefore due to the definition of the coordinate system only a contribution in z direction q_z. This also means that the scattering vector only varies in length but not in the direction during the measurement. This geometrical constrains lead to the fact, that only lattice planes that are oriented parallel to the surface plane contribute to a Bragg reflection. [18]

The detector measures the intensity of the outgoing beam and the data is usually presented as a function of the intensity of 2θ or of the scattering vector q_z. Figure 3.4 shows a XRD measurement with the assigned interplanar distances of the measured Bragg reflections.

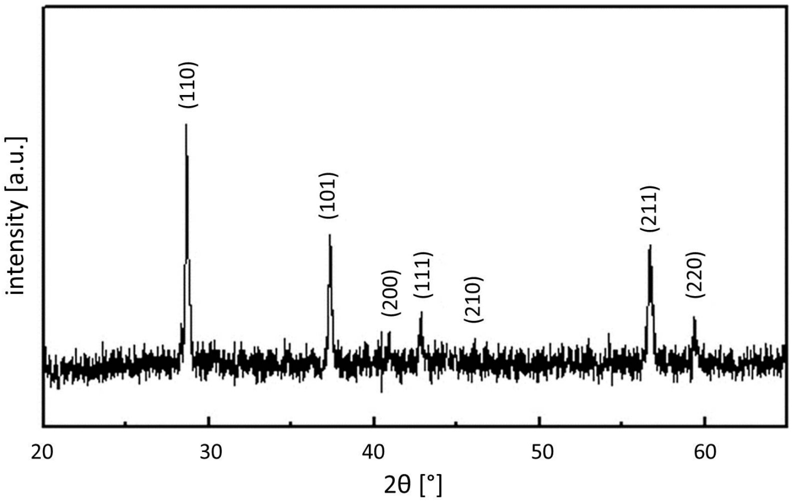

Figure 3.4: XRD measurement with the assigned plane indices. Adapted from [26]

3.3.2 X-Ray Reflectivity

X-ray reflectivity (XRR) is a very similar technique to XRD and also measures $\theta/2\theta$ scans. The difference between a XRD and a XRR measurement is the angular range. While XRD measures up to 2θ angles of many tens of degrees, XRR measures only in the reflectivity regime ($0° - 7°$) but with greater angular resolution. This means that a XRR diffractometer must be able to move the angles of the incoming beam and the detector during the measurement with a very high precision. By measuring $\theta/2\theta$ scans in the reflectivity regime with high angular resolution other effects besides the Bragg peaks can be observed, such as fast oscillating Kiessig or Laue Oscillations. The latters can be used to determine the film thickness and estimate the crystallite size, respectively. Since the critical angle for total reflection θ_c is for most materials below $0.3°$ the incident beam at this low angles gets reflected from the surface rather than scattered from crystal planes. The critical angle can be used to determine the electron density of the sample. At higher angles than the critical angle again Bragg reflections can occur.

Kiessig fringes

Kiessig fringes (see figure 3.5) can be used to determine the thickness of the investigated film. They occur due to interference effects between vacuum/film and the film/substrate interface. By calculating the path difference from geometrical considerations of two beams that are reflected on that interfaces, a simple relation for thickness of the film can be derived:

$$t_{film} = \frac{2\pi}{\Delta q_z} \tag{3.10}$$

Where Δq_z is the period of the fringes in q_z space ($\Delta q_z = q_z^{m+1} - q_z^m$). [18] The period of these fringes gets smaller with increasing film thickness and therefore proper fringes can only be observed up to a film thickness of approximately $200\,nm$.

Scherrer equation

The width of the Bragg peaks can be used to estimate the size of the crystallites via the Scherrer equation.

$$t = \frac{K\lambda}{\beta\, cos\left(\frac{2\theta}{2}\right)} \tag{3.11}$$

Where t is the size of the crystals, K a dimensionless shape factor which is usually close to unity, β the full width at half maximum of the peaks and the θ scattering angle. [27,28]

Laue oscillations

At incident angles above the critical angle the beam can penetrate in the material and can be scattered at the crystal lattice. In the vicinity of a Bragg peak, so called Laue oscillations can be observed. These oscillations occur due to the finite size of the crystals and can be used to estimate the crystal size. [29] A geometrical consideration of this interference effect leads to an analogues relation for the crystal size as for the determination of the film thickness with Kiessig fringes.

$$t_{crystal} = \frac{2\pi}{\Delta q_z} \tag{3.12}$$

Surface roughness

If a rough material is investigated by XRR, the measured intensity at the detector is lower due to more off-specular scattering, which is caused by an uneven surface. This means that the steeper the slope of the measurements is, the rougher is the surface. The roughness can be determined by fitting the data with a proper model.

Electron density

The refraction index for X-ray radiation can be written as: [18]

$$n = 1 - \delta - i\,\beta \tag{3.13}$$

With the dispersion term δ

$$\delta = \frac{\lambda^2\, r_e\, \rho_e}{2\,\pi} \tag{3.14}$$

and the absorption term β, which is approximately zero for X-ray radiation:

$$\beta = \frac{\lambda\,\mu}{4\,\pi} \tag{3.15}$$

With λ the wavelength of the radiation, r_e the Thomson scattering length ($2.815 \cdot 10^{-15}\,m$), ρ_e the electron density and μ the linear absorption coefficient. Since the radiation travels through air ($n_{air} \approx 1$) before hitting the sample, total reflection occurs at low incident angles. Assuming $n_{air} = 1$, Snell's law leads to:

$$cos\,(\alpha_i) = n\,cos\,(\alpha_t) \tag{3.16}$$

With α_i the incident angle of the X-ray beam, α_t the angle of the transmitted beam and n the refraction index of the investigated material. Both angles may be assumed to be very small and therefore the cosine can be approximated with $cos\,(\alpha) \approx 1 - \alpha^2/2$. The absorption term β as well as the quantity $\delta\alpha_t^2/2$ are assumed to vanish, which leads for the angle of the transmitted beam to:

$$\alpha_t = \sqrt{\alpha_i^2 - 2\delta} \tag{3.17}$$

Total reflection, i.e. $\alpha_t = 0$ will be observed if the condition $\alpha_i^2 \leq 2\delta$ is fulfilled. This leads to a relation for the critical angle:

$$\alpha_c = \sqrt{2\delta} = \lambda\sqrt{\frac{r_e \rho_e}{\pi}} \tag{3.18}$$

Therefore, the electron density of the investigated material ρ_e can be calculated from the critical angle or critical scattering vector ($q_z = 4\pi sin(\theta)/\lambda$) respectively. Figure 3.5 shows a XRR measurement with observed critical scattering vectors for the polymer film and the SiO_2 substrate respectively.

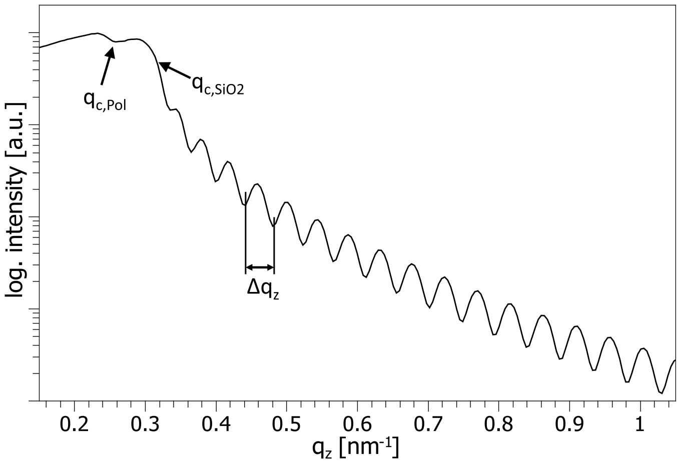

Figure 3.5: XRR measurement with the observed critical scattering vectors of the polymer ($q_{c,Pol}$) and the substrate ($q_{c,SiO2}$) at low incident angles and Kiessig fringes with their indicated period (Δq_z)

3.3.3 Gracing Incidence X-Ray Diffraction

Grazing incidence X-ray diffraction (GIXD) is a surface sensitive method and is used to investigate the in-plane structure of materials. While XRD and XRR measures in specular conditions ($\theta_{in} = \theta_{out}$) to observe Bragg peaks of the out-of-plane structure, GIXD keeps the incident beam constant at an incident angle close to the critical angle of the polymer and the position of the detection changes. Since GIXD does not measure specular scans, the scattering vector **q** has not only the out-of-plane contribution in z-direction q_z but also an in-plane contribution in x and y which is summarized due to symmetry as q_p. In contrast to XRD and XRR, the scattering vector in GIXD measurements is changed in length as well as in its orientation. Figure 3.6 shows the setup of a GIXD measurement equipment.

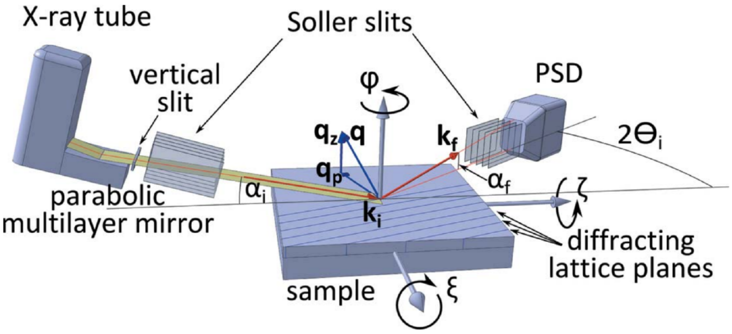

Figure 3.6: Schematic representation of a GIXD equipment. Reprinted from [30]

During a GIXD measurement, the α_{in} is kept constant, while the detector moves along the 2θ semicircle and thus scanning the reciprocal space. This is an important difference between the symmetric $\theta/2\theta$ scan. However, Bragg reflections are found at comparable positions as in $\theta/2\theta$ scans, but in contrast, the angle between the scattered beam and the surface is $2\theta - \alpha$ instead of θ. The measurement data is processed into a so called reciprocal space map, which is a 2D color plot of the measured intensities. While Bragg peaks from 3D crystals appear as "dots" in the space map, Bragg reflections from 2D crystals appear as rods, so called Bragg rods, and Bragg reflections from randomly orientated crystals result in so called Debye Scherrer rings. [18]

3.4 Dynamic Water Contact Angle

Water contact angle measurements investigate the wetability of solid surfaces by the water. Every surface has an unique equilibrium water contact angle. This equilibrium water contact angle is somewhere within the advancing and receding contact angle which can be observed by dynamic contact angle measurements. The advancing contact angle is the maximum contact angle before the droplet contact line advances and the receding contact contact angle is the minimum contact angle right before the droplet contact line recedes. This two contact angles can be observed for example while a droplet slides down on a tilted surface. A more practicable method to measure dynamic contact angles is the sessile drop method which is shown in figure 3.7, where the advancing contact angle is measured while the volume of the drop is increased and the receding contact angle is measured while the volume is reduced. The needle is inserted in the drop as water is added or taken from the drop. [31, 32]

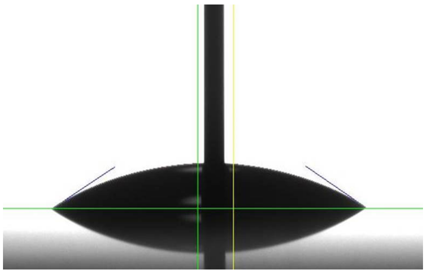

Figure 3.7: Dynamic water contact angle measurement on a silicon substrate with $1.7\,nm$ SiO_2 with the sessile drop method. The horizontal line marks the substrate and underneath the reflection of the drop is visible.

For water contact angles of less than $90°$ the surface is considered hydrophilic and for contact angles larger than $90°$ hydrophobic, which is often observed for polymer surfaces. Fluorinated materials reach contact angles around $120°$. In practice the advancing an receding contact angles show a hysteresis which is effected by the chemical composition, the crystallinity and the roughness of the investigated surface, which is shown in figure 3.8. In contrast to a static contact angle measurement, it is therefore possible to conclude information about the morphology of the surface as well as information about molecular interactions. Chemical heterogeneities on the surface such as the presence of hydrophobic and hydrophilic parts lead to a chain reorientation in the water droplet that the hydrophilic parts stick into the droplet to decrease the surface energy, which leads to a decrease of the receding contact angle and therefore a higher hysteresis. This chain orientation also occurs for non-crystalline surfaces which also increases the hysteresis. Furthermore, the hysteresis always increases with the surface roughness. If an hydrophobic surface also has a "properly-shaped" roughness, non-wetting states, also known as Cassie-Baxter state, can occur due to air pockets under the liquid. These effect can lead to contact angles even higher than $150°$ which is called superhydrophobic. [31–33]

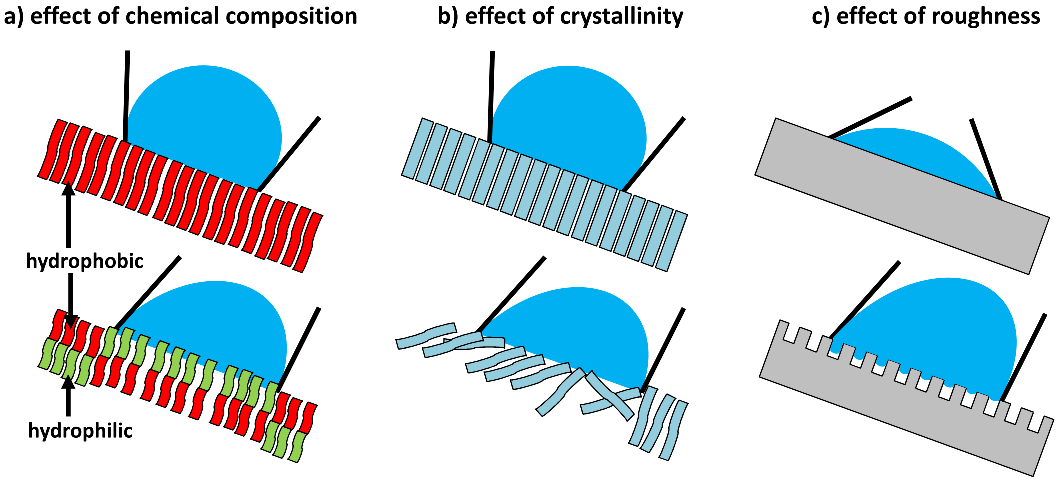

Figure 3.8: Effect on the contact angle hysteresis of the chemical composition (a), the crystallinity (b) (recreated from [33]) and the surface roughness (c).

3.5 Atomic Force Microscopy

Atomic force microscopy (AFM) is a technique for imaging the topography of surfaces with a high resolution, on the order of fractions of a nanometer. [34, 35] Figure 3.9 shows a schematic representation of an AFM setup.

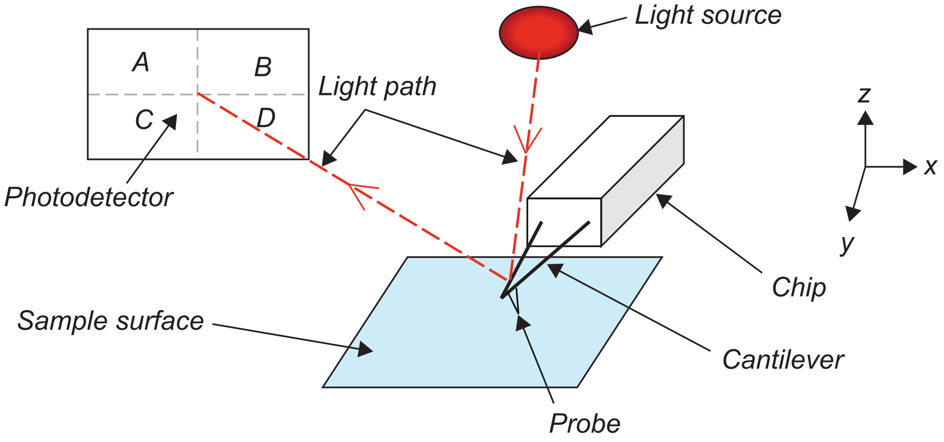

Figure 3.9: Schematic representation of an AFM setup. Reprinted from [34]

The AFM uses a micro-fabricated cantilever made of silicon or silicon nitride with a sharp tip that interacts with the surface of the sample. When the tip is brought close to a surface, forces such as mechanical contact force, "van der Waals" force etc. lead to a deflection or a change of the oscillation amplitude (depending on the imaging mode) of the cantilever. The cantilever scans the surface in xy-direction while its deflection or oscillation amplitude is measured with an optical tracking system which uses a segmented detector to track the reflection of the light beam. Detected changes in the cantilever deflection or oscillation are corrected by adjusting the cantilever in z-direction with a feedback-controlled piezo. The height of a given xy-coordinate is calculated from the correction. There are various imaging modes available for the AFM but the most common are:

Contact mode imaging

In contact mode imaging, the tip is "dragged" across the surface and the topography of the surface is measured using the deflection of the cantilever.

Tapping mode imaging

In tapping mode imaging the cantilever oscillates and the amplitude of oscillations is decreased by forces between the tip and the surface when the tip approaches the surface. The feedback mechanism adjusts the height of the tip to maintain a constant amplitude which is recorded to recreate the topography of the surface.

Non-contact mode imaging

In non-contacting mode imaging, the tip also oscillates but with a smaller amplitude than in the tapping mode. When the tip comes close to the surface long range interactions such as "van der Waals" forces between the tip and the sample cause a detectable shift of the frequency of the cantilever's oscillation. This shift is used to calculate the topography of the surface.

3.6 Scanning Electron Microscopy

Scanning electron microscopy (SEM) is a technique to investigate surfaces of a sample by scanning it with a finely focused beam of electrons. [36] These electrons, the so called primary electrons, interact with the sample and produce various signals that can be detected to gain information about the sample's surface topography and the composition. The possible interactions are shown in figure 3.10. The most commonly used signals are secondary electrons, backscattered electrons and the characteristic X-ray radiation.

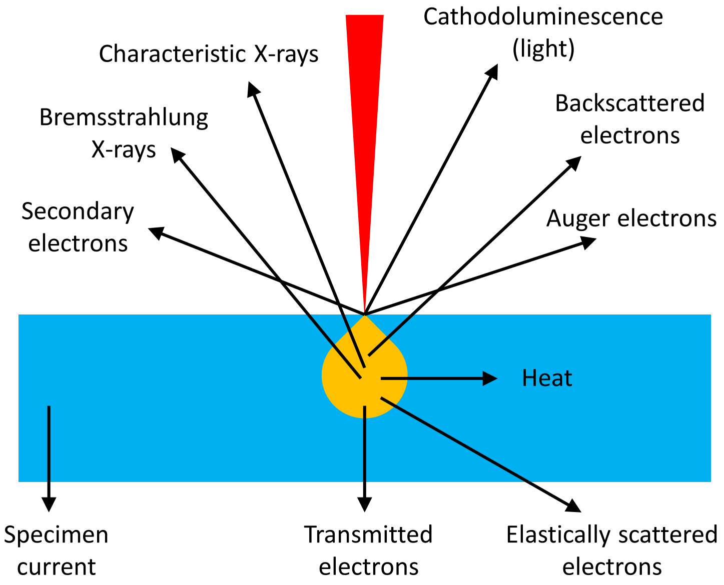

Figure 3.10: Interactions of the primary electron beam with matter. Recreated from [36]

Secondary electrons (SE)

These electrons have a low energy ($< 50\,eV$), whereby they can only leave the sample close if they are created close to the surface. This leads to a high spatial resolution. The brightness of the of the signal and therefore of the pixel in the image depends on the amount of detected secondary electrons. Because steep surfaces and edges tend to be brighter, a high topographical contrast as well as three dimensional appearance is achieved. Due to their low energy and the resulting low interaction volume in the sample, secondary electrons achieve the highest spatial resolution which is in the low nanometer scale.

Backscattered electrons (BSE)

Backscattered electrons are high energy electrons from the primary electron beam, that are back-scattered out of the sample by elastic scattering. The amount of backscattered electrons strongly depends on the mean atomic number of the elements that are present in the investigated area of the sample. This leads to a high contrast between different chemical compositions.

Characteristic X-ray radiation

The interaction of the primary electron beam with the sample can lead to X-rays with wavelengths that are characteristic for a certain element. This X-ray radiation may be detected to perform a qualitative and quantitative investigation of the sample's composition of elements.

3.7 Electrochemical Impedance Spectroscopy

Electrochemical impedance spectroscopy (EIS) is a powerful technique for studying fuel cells and has been widely used for testing proton exchange membranes. EIS measures the impedance of a system by applying a usually very small AC signal to it. [16] In contrast to a metal, where the positive ions are fixed in the crystal lattice, in a fuel cell membrane hydrogen ions hence protons can move and contribute to an electrical current. Figure 3.11 shows the proposed equivalent circle for a PEM fuel cell.

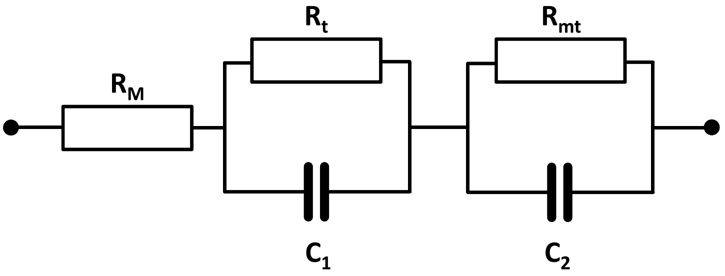

Figure 3.11: Proposed equivalent circuit for a PEM fuel cell. Recreated from [16]

Where R_M represents the membrane resistance, R_t the charge transfer resistance with the associated catalyst layer capacitance C_1 and R_{mt} represents the resistance related to the mass transfer process of gas diffusion (O_2 and H_2) in the catalyst layers, with the associated capacitance C_2. [16]
If EIS is not performed on a complete fuel cell but only on the membrane, the equivalent circuit differs, but capacitances and inductances, e.g. from the electrode wires, impact the impedance. The in-plane conductivity can be measured with a four-electrode setup, which is shown in figure 3.12. The membrane with a width W and a thickness T is contacted by two outer electrodes which supply the AC signal and two inner voltage-sensing electrodes that have a distance of L. [37]

Electrochemical impedance spectroscopy is usually measured from the low Hz range up do several kHz. At certain frequencies the imaginary part of the impedance equals zero, where the measured resistance equals the resistance of the parallel circuit of the membrane and the solution resistance. Since protons can also travel through the solution to some extend, accurate measurements of the membrane re-

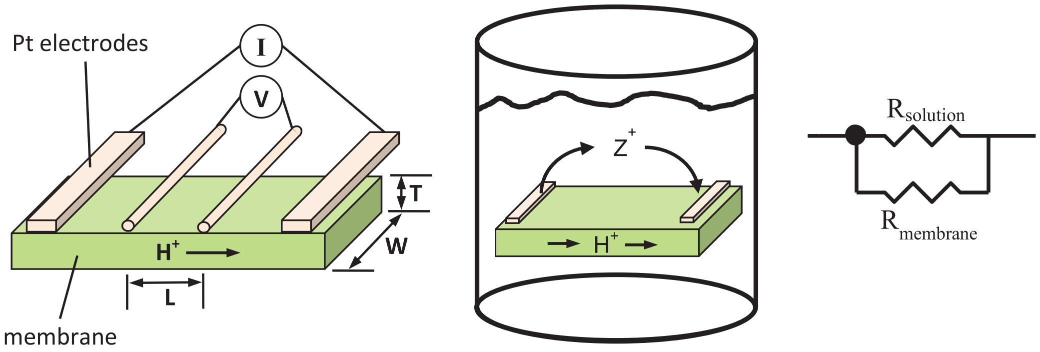

Figure 3.12: Illustration of a four-electrode in-plane conductivity measurement. Reprinted from [37]

sistance require $R_{solution} >> R_{membrane}$. If $R_{solution} >> R_{membrane}$, the resistance of the solution can be neglected due to (3.19). [37]

$$R_{membrane} = \left(\frac{1}{R_{total}} - \frac{1}{R_{solution}} \right)^{-1} \tag{3.19}$$

The conductivity of the membrane can be calculated via:

$$\sigma = \frac{L}{R_{membrane} \, W \, T} \tag{3.20}$$

EIS measurements can also be carried out in situ during fuel cell operation, which allows to gain more information about the membrane performance. [16]

4 Results and Discussion

4.1 Perflourinated Membranes - MAA-PFDA Copolymers

In the first approach proton copolymers were synthesized out of the hydrophilic methacrylic acid (MAA) and the hydrophobic 1H, 1H, 2H, 2H,-perflourodecyl acrylate (PFDA). A summary of this results can be found in the forthcoming publication [38]. MAA has a functional $COOH$ group that, when immersed in water, becomes an ionic COO^- group which allows the transport of protons. The use of PTFE is justifed because it was shown in literature that PFDA has the same crystal structure as PTFE, that is used to create the hydrophobic semicrystalline matrix in Nafion®. [39] PFDA has a fluorinated backbone, which makes the molecule hydrophobic whereby it ensures the stability of the polymer in water. The used initiator was tert-butyl peroxide(TBPO) which has a labile $O-O$ that was thermally composed in the reactor to create primary radicals. The chemical structure of this materials is shown in figure 4.1. Polymers with different chemical composition of this two monomers were obtained by changing the monomer flow rates in order to tune the ratio of fluorinated over carboxylic groups. The used flow rates and the corresponding P_M/P_{sat} can be found in table 6.1 in the experimental section for the MAA-PFDA copolymers. The consequent MAA fraction f_{MAA} on the surface (calculated from (3.9)), the fracion of MAA in the copolymer F_{MAA} (which was determined by FTIR spectroscopy), as well as the obtained deposition rates can be found in table 4.1.

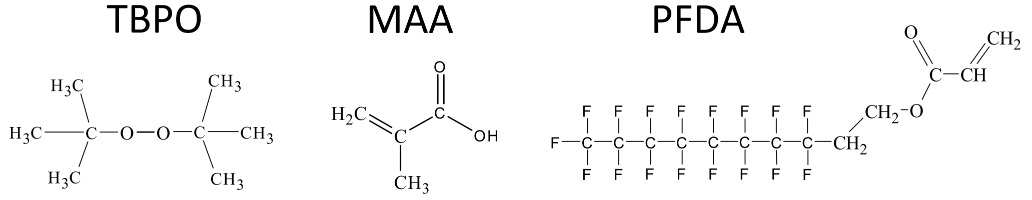

Figure 4.1: Chemical structures of TBPO, MAA and PFDA

4.1.1 Chemical Composition

In order to determine the chemical composition of the polymers, the films were investigated by FTIR spectroscopy, which is shown in figure 4.2. As the MAA fraction in the copolymer increases, the absorptions of the fluorinated pendant chains (symmetric and asymmetric CF_2 stretching at $1205\,cm^{-1}$ and $1233\,cm^{-1}$, respectively and the $CF_2 - CF_3$ stretching at $1150\,cm^{-1}$) and of the functional group $COOR$ at $1741 cm^{-1}$ decrease in intensity while the contrary applies for the peak of the $COOH$ group at $1706\,cm^{-1}$.

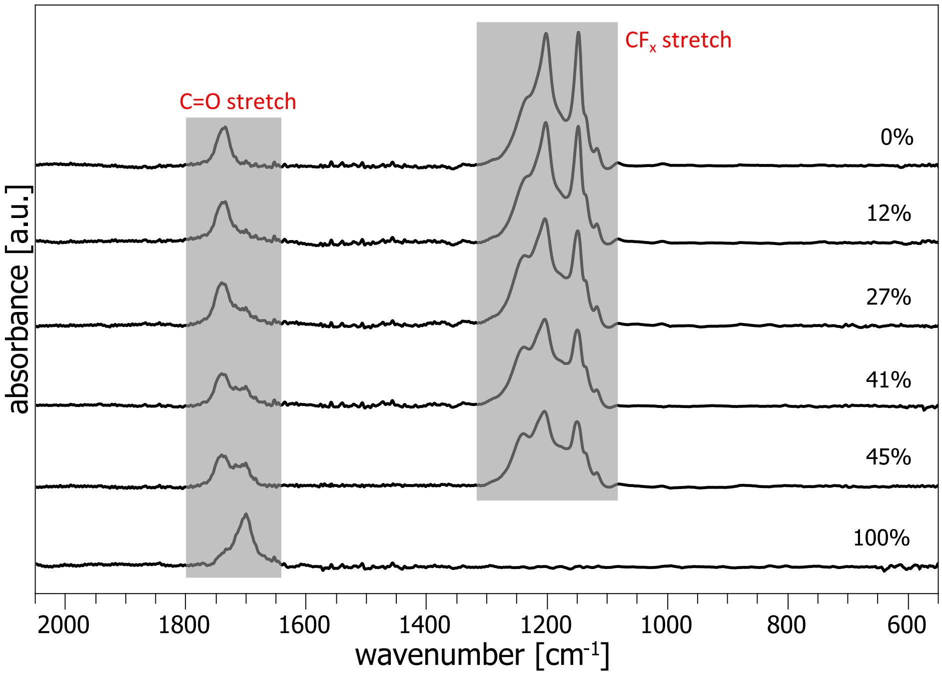

Figure 4.2: FTIR-Spectroscopy of different copolymers in the range from $2050 - 550\,cm^{-1}$. The labels give the actual fraction F_{MAA} in the polymer.

The absorption of the $C = O$ stretch is caused by both, the $COOH$ group of the MAA and the $COOR$ group of the PFDA. A shift of this peak can be observed from $1706\,cm^{-1}$ (MAA - $COOH$ group) to $1740\,cm^{-1}$ (PFDA - $COOR$ group) due to the higher mass of the $COOR$ group. The areas of the individual contributions to the peak depend on the fraction of each monomer in the copolymer. The peaks in the range $1100 - 1250\,cm^{-1}$ are characteristic features of the fluorinated groups and were only observed for PFDA containing polymers.

Figure 4.3 shows a non-linear least-square regression of the carbonyl peak using two Gaussian components for the $COOH$ and $COOR$ groups. The actual fraction

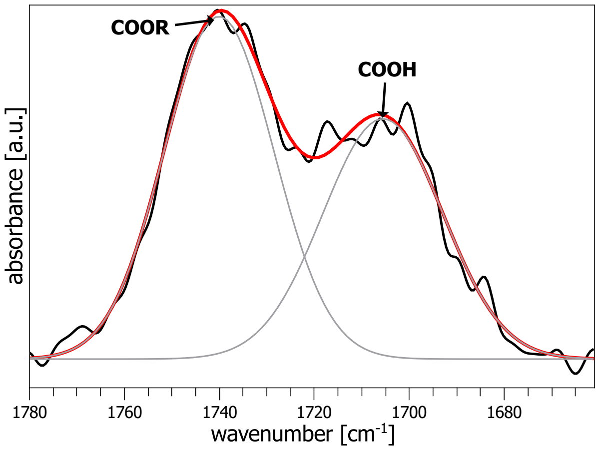

Figure 4.3: Multiple Gauss fit of a carbonyl peak.

of MAA and PFDA in the copolymer was determined by calculating the ratio of the area of the individual Gauss component to the total area. Since the $COOH$ groups only come from MAA and the ester groups $COOR$ only from PFDA, the area under each Gauss component was used to determine the percentage of MAA in the film (referred as F_{MAA}). Depending on the reactivity of the monomer, the actual percentage of monomer units in the copolymer is usually different from the one calculated with the P_M/P_{sat} (f_{MAA}). [12] The last column of table 4.1 shows the actual percentage, F, of MAA in the copolymer, calculated from the FTIR COOH contribution. It is noteworthy noticing that F_{MAA} increases with f_{MAA}, which is shown in figure 4.4.

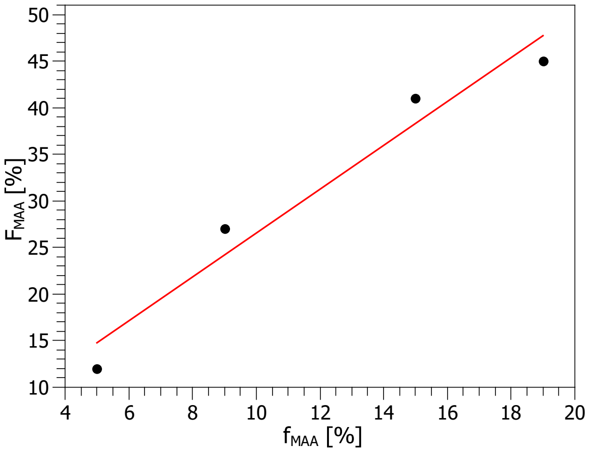

Figure 4.4: Plot of the fraction of MAA in the copolymers F_{MAA} versus the fraction of MAA at the surface $fMAA$.

The obtained deposition rates (table 4.1) were ranging from 2.3 to $6.5\,nm/min$, comparable to previous iCVD deposition rates from the same couple of monomers in the crystalline regime. [39] The deposition rates generally increased with a higher total monomer flow rate.

Table 4.1: Deposition rates and MAA fraction on the surface (f_{MAA}) and in the copolymer (F_{MAA})

Sample	Dep. rate [nm/min]	f_{MAA} [%]	F_{MAA} [%]
A	2.3	0	0
B	3.1	5	12
C	4.6	9	27
D	5.7	15	41
E	6.5	19	45
F	3.7	100	100

4.1.2 Crystallographic Investigation

Various X-ray based methods were used to investigate the structure of the polymers. Since each of these methods uses X-ray sources with different wavelengths the diffractograms are reported in terms of scattering vector q_z instead of the scattering angle 2θ. The big advantage of using the scattering vector is that the position does not depend on the wavelength of the X-ray source and therefore makes it easier to compare the figures. The scattering vector q_z is obtained from the scattering angle via (2.13). The magnitude of $\mathbf{q}_z$ is correlated with the interplanar plane distance d_{hkl} via (2.20). Figure 4.5 shows the XRR diffractograms of the films. The intensity is plotted in logarithmic scale and the curves are shifted for clarity.

Pure PFDA polymers showed strong 1^{st} and 2^{nd} order Bragg peaks of the (001) plane, at $q_z = 1.98\,nm^{-1}$ and $q_z = 3.92\,nm^{-1}$, respectively. These peaks correspond to an interplanar distance of $3.19 \pm 0.02\,nm$. The peaks occur due to a organization of the fluorinated chains into a bilayer structure (see scheme 4.7). It was shown before that PFDA crystallizes into an ordered lamellar structure, called smectic B phase when deposited by iCVD. [11, 39] The interplanar distance $3.19\,nm$ corresponds to the length of the double layer, of fluorinated chains. On the left and right hand side of the Bragg peaks, in the PFDA homopolymer, Laue oscillations were observed. The intensity of the Bragg peaks decreases with the MAA fraction in the copolymer, which can be explained with some loss of crystallinity. Also

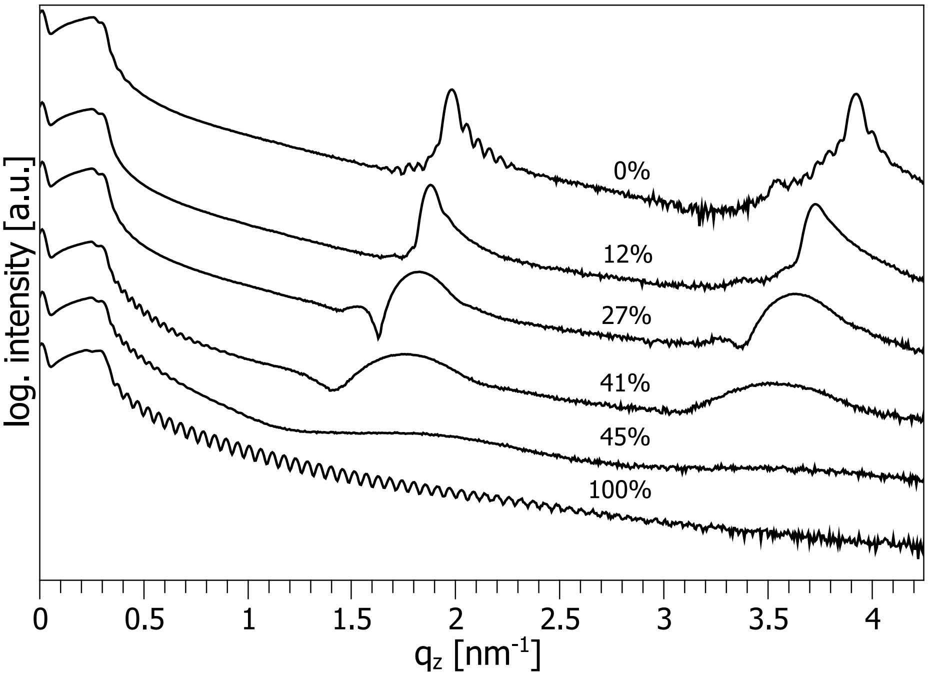

Figure 4.5: XRR measurements of the polymers. The labels give the percentage of MAA in the polymer (F_{MAA}).

other authors have shown that copolymers of PFDA do not retain the crystallinity degree of the PFDA homopolymer, when a comonomer is added. [40] The Bragg peaks are also broadened which indicates that the crystallite size decreases. The MAA homopolymers showed no Bragg peaks, as expected. Indeed, since MAA is a small molecule it is more likely to give amorphous polymers than crystalline. The observed Kiessig fringes in the pure MAA polymer XRR profile can be used to determine the film thickness. These fringes disappear for films with a MAA fraction $\leq 27\%$ probably due to roughening of the surface.

It can be observed in figure 4.5 that the Bragg peaks shift to lower angles with increasing MAA fraction, which demonstrates an increase of the interplanar distance. The interplanar distance, d, calculated from the position of the Bragg peaks is plotted in figure 4.6 as a function of F_{MAA}. The exact peak position and the full width at half maximum intensity ($FWHM$) were obtained by fitting the Bragg peaks with a Gaussian curve. Since the peaks of the film with 45% MAA were very weak and broadened it was not possible to obtain a proper fit. The $FWHM$ was used to estimate the crystal size (t) using the Scherrer equation (3.11).

The shape factor K was assumed to be 1. Also the estimated crystal size is plotted

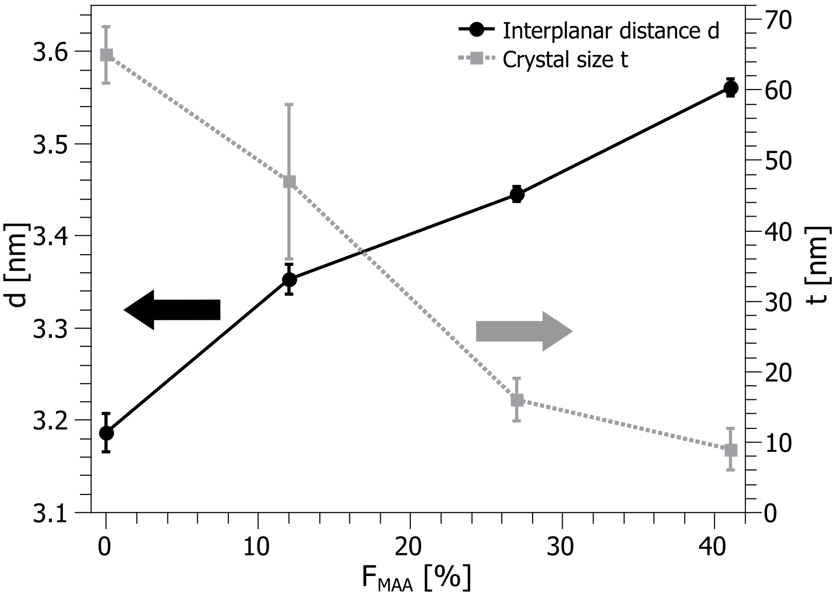

Figure 4.6: Plane distance and crystal size as a function of the MAA percentage in the copolymer (F_{MAA}).

in figure 4.6 as a function of F_{MAA}. The interplanar distance significantly increased from $3.19\,nm$ to $3.56\,nm$, while the estimated crystal size decreased from $65\,nm$ to $9\,nm$. The interplanar distance increase with the MAA fraction proves that there is no phase separation among MAA domains and PFDA domains in the copolymer. Kinetic studies have proven that MAA-PFDA copolymers have a moderate alternate composition in terms of MAA units linked to PFDA units. [12] XRR confirms this theory, indeed, in case of a phase separation between the crystalline PFDA and the amorphous MAA, the peak would decrease in intensity with increasing MAA fraction, but would always be observed at the same q_z. An alternate polymer composition, without phase separation between MAA and PFDA domains, is difficult to achieve with other techniques, due to their big difference in solubilities. With the iCVD method, this problem is circumvented. In scheme 4.7, a model is proposed for the PFDA homopolymer and the MAA-PFDA copolymer. It is hypothesized that the MAA molecule turns on the outside of the bilayer structure, increasing the length of the repeat unit and thus the interplanar distance of the copolymer. This kind of phase segregation is probably caused due to the chemical heterogeneity of the MAA and the PFDA. The fluorinated chain bends over to fill the occurring empty space, which leads to a more disordered state and smaller crystals. This model will be verified by Molecular Dynamics simulations.

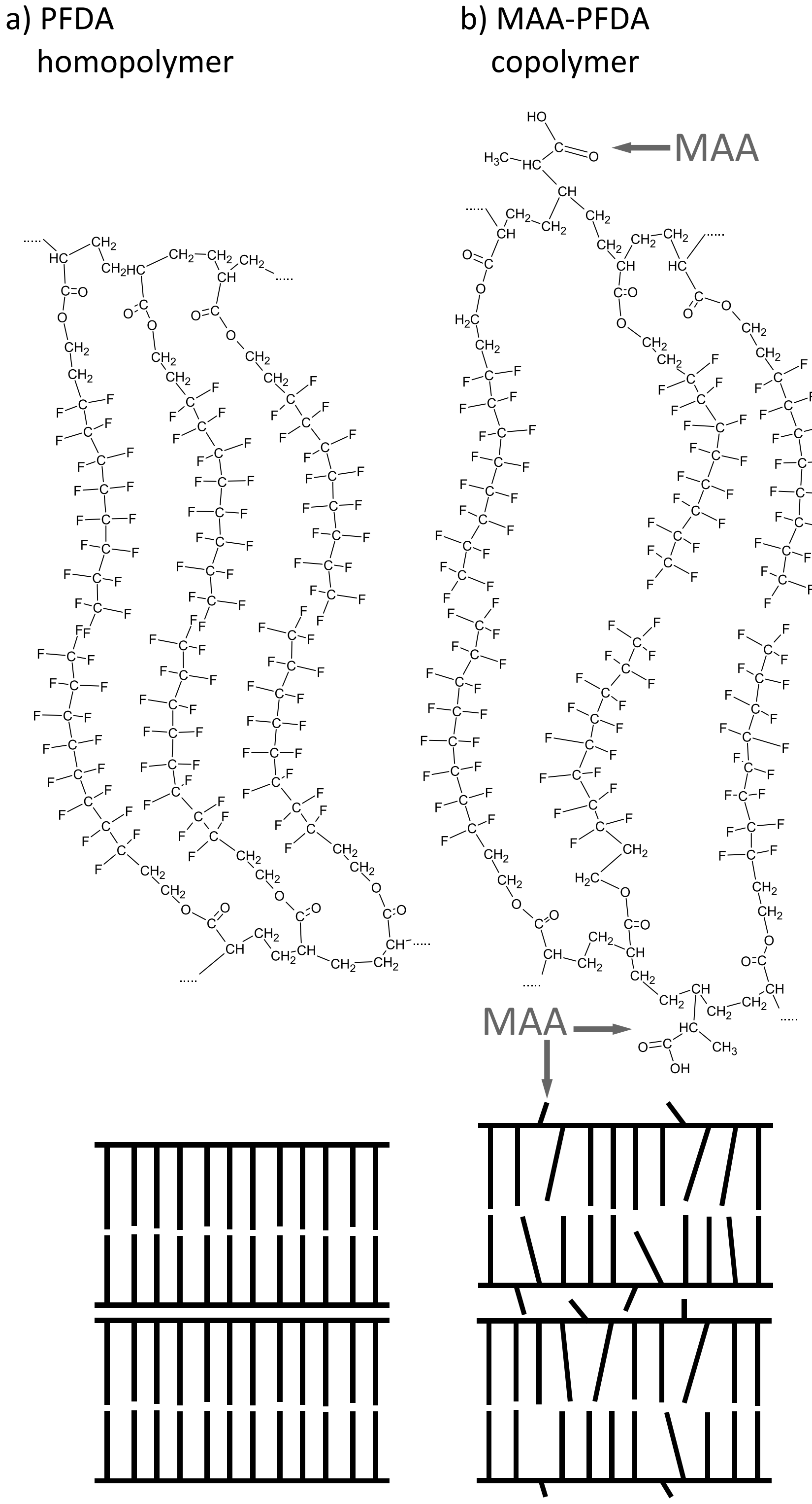

Figure 4.7: a) Bilayer structure of the PFDA homopolymer b) Hypothetical model for the MAA-PFDA copolymer structure.

The cluster-network model that was proposed for hydrated Nafion® describes the formation of ionic clusters that are interconnected by ionic channels. [7] The MAA-PFDA polymers were not investigated in the hydrated state and therefore it was not possible to observe peaks that would indicate such a formation of ionic clusters. But indeed, the hypothesised model would already allow the formation of ionic channels between the bilayers where only MAA chains are present. The measured increase of the interplanar distance for the copolymer with 41% MAA is $0.37\,nm$, which is approximately the length of the MAA molecule. This means in the copolymer with 41% MAA fraction, the MAA molecules stand upright, leading to a wider ionic channel, which could be beneficial for the proton conductivity. To investigate if there is a preferred orientation of the crystals or if they are oriented randomly, XRD measurements were carried out at different tilt angles (see figure 4.8).

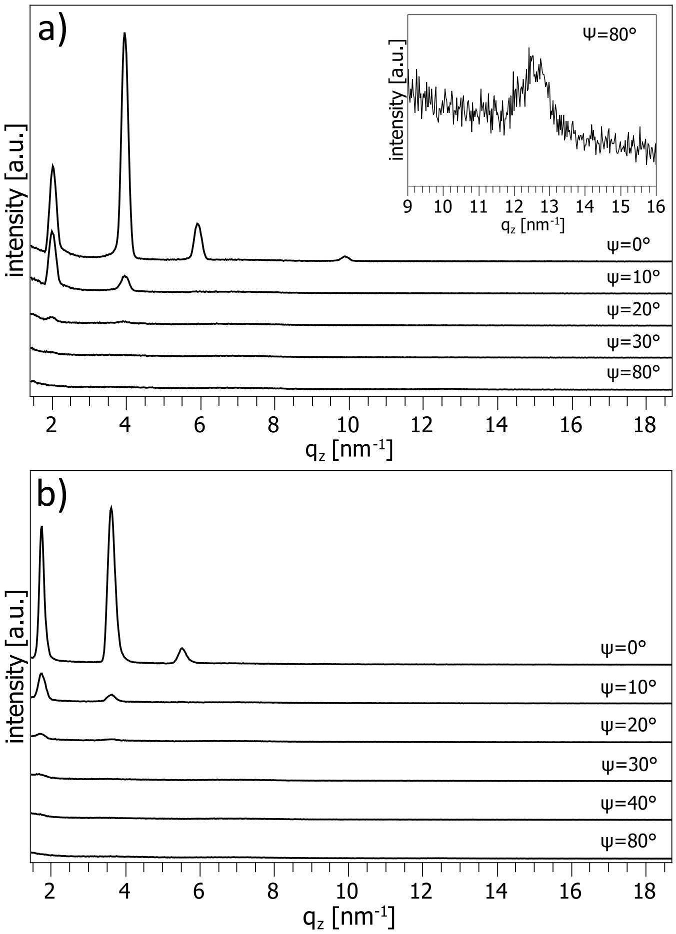

Figure 4.8: $\theta - 2\theta$ scans at different tilt angles of the samples of a PFDA homopolymer (a) and a MAA-PFDA copolymer with 12% MAA fraction (b). The inset in (a) shows a zoom in the $9 - 16\,nm^{-1}$ range of the $\theta - 2\theta$ scan at a tilt angle of $80°$.

Only crystals with net planes perpendicular to the scattering vector contribute to the Bragg peak signal, whereby peaks at $\Psi = 0°$ occur only from crystals which are oriented perpendicular to the surface. At $\Psi = 0°$ the observed peaks occur due to the orientation into bilayers (scheme 4.7). The peaks observed for the PFDA homopolymer in 4.8a at 1.98 and $3.92\,nm^{-1}$ are the same 1^{st} order and 2^{nd} order Bragg peaks that are visible also in figure 4.5. The 3^{rd} and 5^{th} orders are also visible in figure 4.8a at 5.92 and $9.88\,nm^{-1}$. For the copolymer with $12\,\%$ MAA fraction 1^{st} and 2^{nd} order peaks were observed at 1.88 and $3.73\,nm^{-1}$ analogously to the XRR measurements, as well as a 3^{rd} order peak at $5.60\,nm^{-1}$. The intensity of the Bragg peaks of the bilayer structure decreases fast with an increase in the tilt angle and the peaks are no longer visible at $\Psi = 30°$ and $\Psi = 40°$, respectively or higher. It is evident that there is indeed a preferred orientation of the crystals at $\Psi = 0°$ but the orientation is distributed in the range from $0 - 40°$. This preferred orientation of the crystals was observed for all crystalline polymers. The preferential orientation of the crystals perpendicular to the substrate surface implies that the ionic channels are oriented parallel to the surface. The inset of figure 4.8a shows a zoom of the diffractogram measured at $\Psi = 80°$. A small peak is visible at $q_z = 12.5\,nm^{-1}$ which indicates an in-plane order. According to literature, the in-plane structure of PFDA is hexagonal. [39] The measured peak at $q_z = 12.5\,nm^{-1}$ corresponds to an interplanar distance of $0.50\,nm$. This in-plane distance leads to a lattice constant of $0.58\,nm$ (scheme 4.9). This in-plane peak was not observed for the copolymer films.

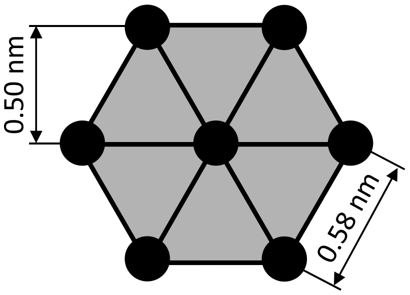

Figure 4.9: Hexagonal in-plane structure of pure PFDA polymers. The measured interplanar distance of $0.50\,nm$ corresponds to a lattice constant of $0.58\,nm$

To gain more information about the crystal structure, GIXD measurements were performed and the results are shown in figure 4.10. The PFDA homopolymer (4.10a) showed a strong peak at $q_p = 12.5\,nm^{-1}$ that matches with the observed XRD peak at $\Psi = 80°$ and confirms that there is an in-plane order with an interplanar distance of $0.50\,nm$. The fact that the GIXD measurement for the PFDA homopolymer has shown a peak rod rather than a peak means that PFDA crystallizes in a 2D crystal where the planes are not correlated. All these data confirms that PFDA crystallizes in a smectic B phase (scheme 4.11b).

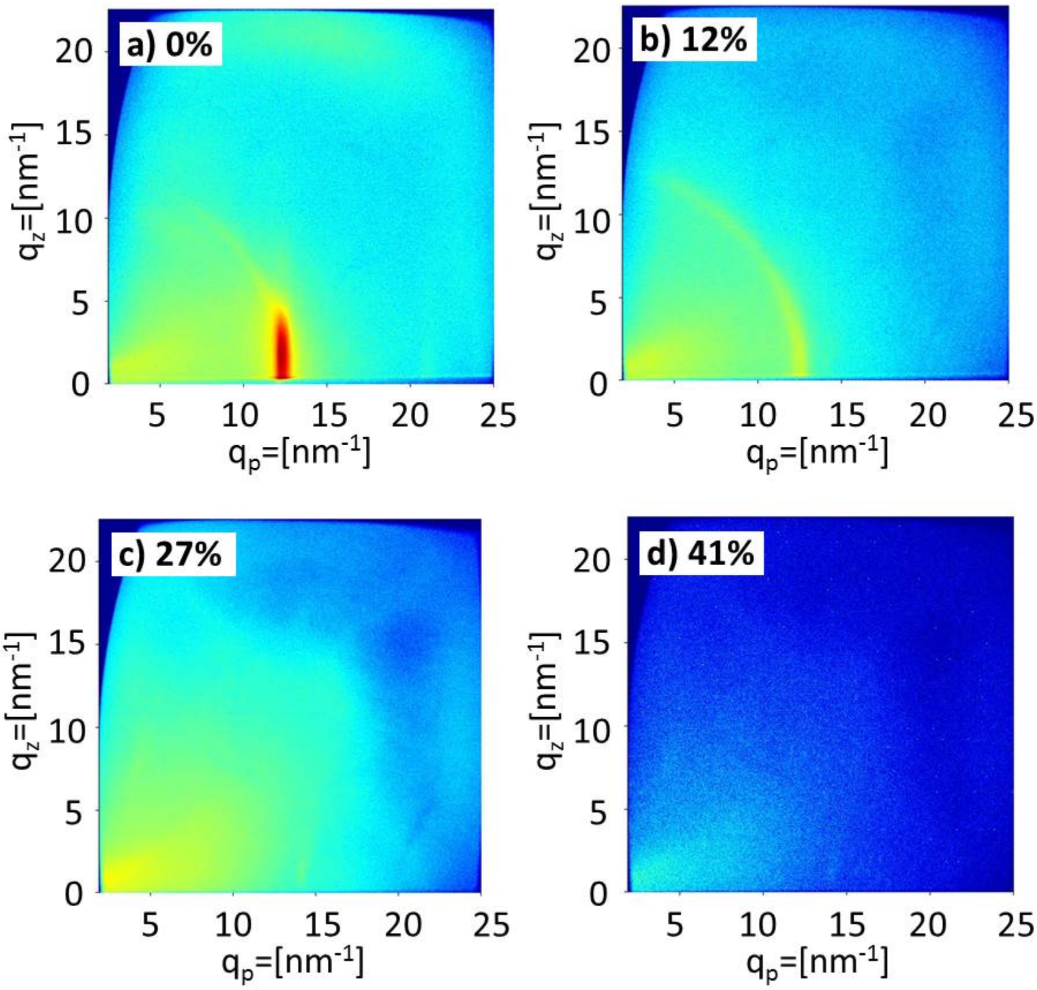

Figure 4.10: Grazing incidence X-ray diffraction (GIXD) measurements. The labels correspond to the actual fraction F_{MAA} in the polymer.

The peak rod is no more observable for the 12% MAA film, meaning that there is no in-plane order for the MAA-PFDA copolymers. A weak Debye-Scherrer ring is visible for the samples with $F_{MAA} = 0\%$ and 12%, which demonstrates that there are randomly orientated crystals together with the smectic phase. At higher MAA fraction (4.10c and 4.10d) also the Debye Scherrer ring disappears completely and the films showed only amorphous scattering. The absence of in-plane order but the evidence of lamellar organization with preferential orientation are characteristics of a smectic A phase (scheme 4.11a). MAA-PFDA copolymers crystallizes in a smectic A phase with a layered structure and a preferred orientation of the polymer chains. PFDA homopolymers crystallizes in a smectic B phase 4.11b which has besides a layered structure and a preferred orientation of the crystals also a hexagonal in-plane structure.

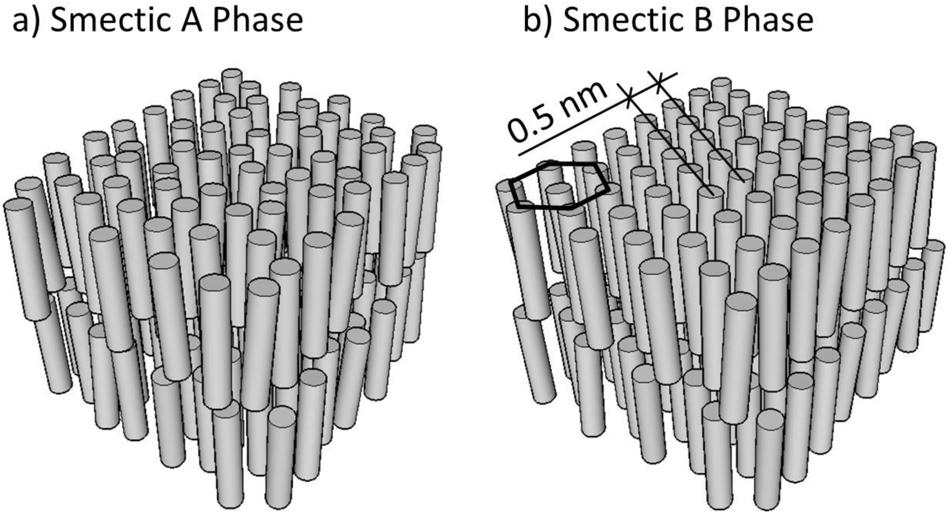

Figure 4.11: Schematic representation of a smectic A phase (a) and a smectic B phase with a hexagonal in-plane order and a interplanar distance of $0.50\,nm$ (b).

4.1.3 Surface Morphology

The surface morphology of the films was investigated with AFM in tapping mode. Figure 4.12 shows the AFM topographical images of the PFDA homopolymer and the copolymer with $12\,\%$ and $27\,\%$ MAA fraction. In contrast to the homopolymer, which showed the presence of sharp and high islands at defined sites with a low density, the copolymer showed a more molehill-like morphology (i.e. large features). The observed size of the features as well as the the RMS roughness of the films decreased with increasing MAA fraction in the polymer. The RMS roughness of the PFDA homopolymer was $24.4\,nm$ and decreased for the copolymers with the MAA fraction (figure 4.12d). The MAA homopolymer was very smooth with a roughness of $0.8\,nm$. Also the copolymers with high MAA content, e.g. with $45\,\%$ MAA were smooth and had a roughness of $1\,nm$. This confirmed the XRR observation, were Kiessig fringes were only visible for films with $41\,\%$ MAA or higher.

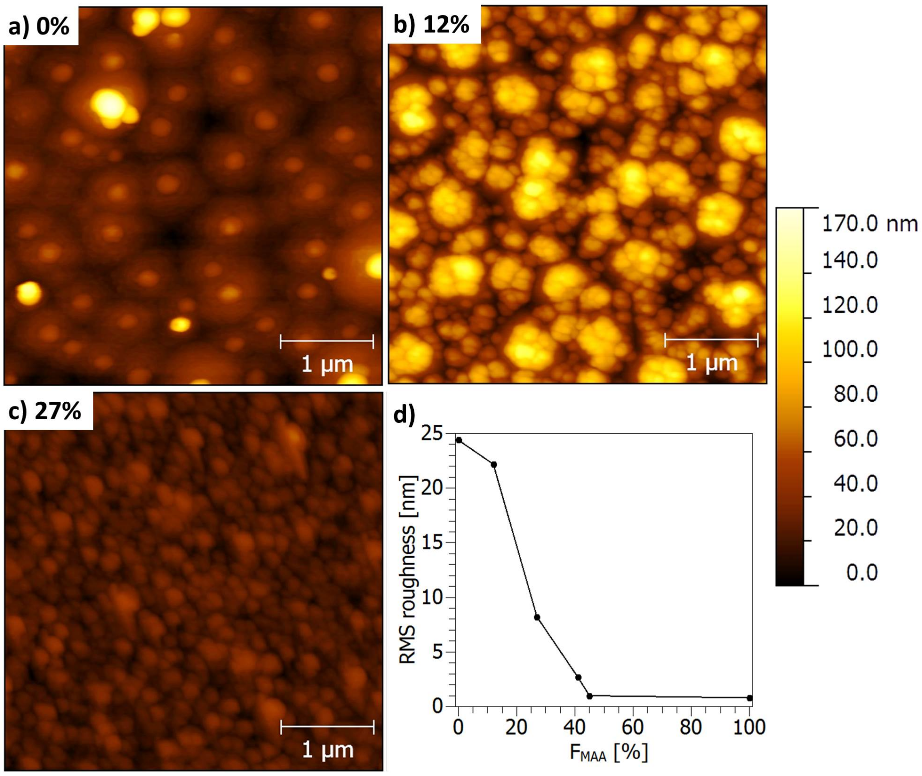

Figure 4.12: Topographical AFM investigation of the films (a-c) with constant height scale and a plot of the RMS surface roughness (d). The labels correspond to the actual fraction F_{MAA} in the polymer.

4.1.4 Dynamic Water Contact Angle

Dynamic water contact angles were measured to investigate the ability for chain reorientation. Advancing (WCA_{adv}) and receding (WCA_{rec}) contact angles on the copolymer films and on PFDA homopolymer are shown in figure 4.13. The contact angle on the MAA homopolymer decreased rapidly with time and the film was almost instantly diluted by the water. Therefore there are no measurements available for the MAA homopolymer.

The advancing contact angle for the PFDA homopolymer was $124°$ and increased for the copolymer with $12\,\%$ MAA to $143°$. This increase could be caused by the change in the smectic phase. Since the $12\,\%$ MAA is less crystalline, the chains are more randomly oriented and more hydrophobic CF_3 groups can be exposed on the surface which increases the WCA. By further increasing the hydrophilic MAA components the advancing WCA slightly decreased to $127°$. The receding WCA for the PFDA homopolymer was $97°$ and steady decreased with the MAA fraction leading

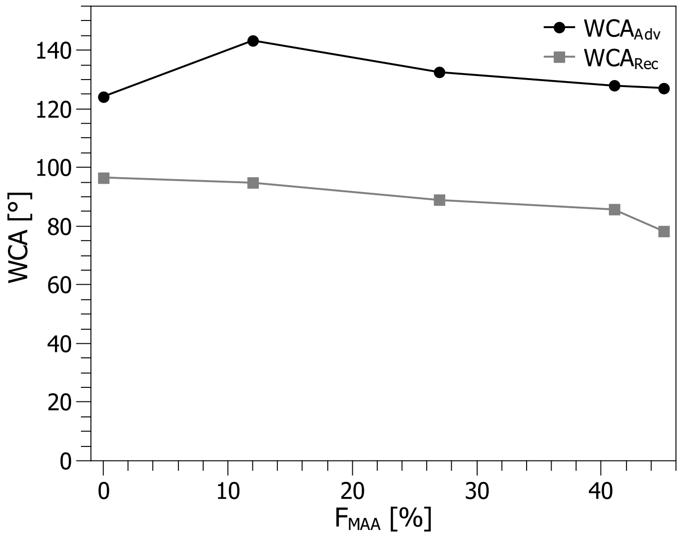

Figure 4.13: Advancing and receding water contact angles measured for the MAA-PFDA copolymers, varying the MAA fraction.

to an increase in hysteresis from 27° to 49°. The increase in hysteresis can be due to several factors. (i) The copolymers are less crystalline than the PFDA homopolymer. This means they can relatively more easily re-orient to expose hydrophilic groups inside the drop of water. (ii) the copolymers are very likely to have surface chemical heterogeneities due to the presence of the MAA units in addition to PFDA. (iii) The structure of the surface, that was investigated in the previous section, can also affect this behaviour, i.e. if there is a Cassie-Baxter regime, the morphology is such that it enhances the hydrophobicity of the surface but probably the spacing among the surface features is high related to their depth, so water fills in the gaps and sticks on the surface.

4.1.5 Proton Conductivity

The thickness of a proton exchange membrane is usually around $100\,\mu m$, which would take a long time to deposit with the obtained deposition rates. To avoid depositions over several days which would probably lead to problems with non-constant monomer flow rates, the films were deposited on a $63\,\mu m$ thick porous PTFE carrier film, that would also allow to test the membrane in an actual fuel cell. During the deposition of this films, the thickness was monitored with Laser interferometry on a silicon wafer until a thickness of $1\,\mu m$ was reached. Since it is practicably impossible to measure the film thickness on this porous PTFE carrier, it was estimated to be equal to measured thickness on the silicon wafer. Discrepancies in the temperature conditions during the depositions between the silicon substrate and PTFE film could have led to differences in the deposited film thickness, which would lead to significant errors in the calculation of the conductivity from the measured membrane resistance. Since our model suggests that the ionic channels are oriented parallel to the surface, the in-plane proton conductivity was measured using electrochemical impedance spectroscopy. For the used measurement setup the resistance of the water was around $270\,k\Omega$. Since the film thickness was only $1\,\mu m$, the measured resistance of the membranes was rather high, ranging between $48\,k\Omega$ and $138\,k\Omega$. Therefore the water resistance could not be neglected and was measured additionally for every membrane measurement and the measured membrane resistance was corrected via (3.19).

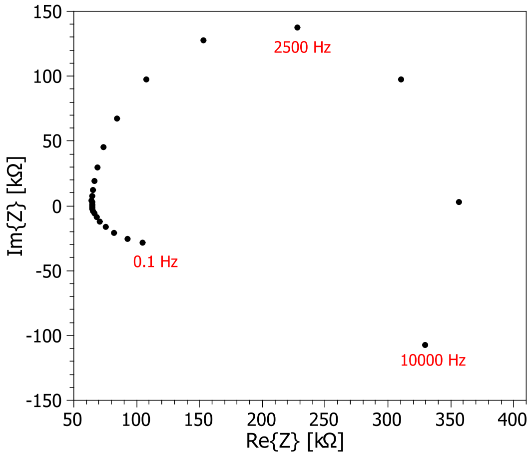

Figure 4.14: Nyquist plot of the EIS measurement of a copolymer with $27\,\%$ MAA fraction

Figure 4.14 shows a so called Nyquist plot, which represents the imaginary part of the impedance versus the real part of the impedance at the different frequencies. At the points were the imaginary part disappears, the measured resistance equals the resistance of the parallel circuit of the membrane and the water resistance. To make the measurements comparable, the conductivity for all copolymers was determined in the low frequency range at a frequency of $10\,Hz$. The results for the proton conductivity are summarized in table 4.2.

Table 4.2: Proton conductivity σ of MAA-PFDA membranes, calculated via (3.20)

Sample	$F_{MAA}[\%]$	$\sigma\ [mS/cm]$
B	12	12
C	27	41
D	41	55
E	45	46

As a reference, also the conductivity of Nafion®115 was measured as $126\,mS/cm$, which is in agreement with literature values. While the amount of ionizable groups in the copolymer with $12\,\%$ MAA fraction is low and therefore the conductivity was only $12\,mS/cm$ for this copolymer, the conductivity was significant higher for films with a higher MAA fraction and reached a maximum of $55\,mS/cm$ for the copolymer with $41\,\%$ MAA fraction. Beside the higher fraction of ionizable groups, also the higher width of the ionic channels, which was discussed previously, could have led to this high proton conductivity. Proton conductivity values in this range were reported also in a preliminary study on MAA-PFDA copolymers. [12] These ionic channels are able to contribute to the proton transport since they are oriented in-plane between the bilayers and also the conductivity was measured in-plane. It was shown in literature that the orientation of the bilayers can be tuned with the depositions conditions [39] and therefore it should be possible to orient the ionic channels in through-plane direction, which would be important for the application as a PEM. This results are very promising and since the proton conductivity was measured at room temperature it can be expected that it would be even better at higher temperatures. But as already mentioned, the estimation of the film thickness and the influence of the water resistance could have led to big errors and therefore more experiments on thicker membranes are necessary to confirm the results.

4.2 Hydrocarbon Membranes - MAA-DVB Coplymers

In the second approach proton conductive polymers were synthesized using only hydrocarbon monomers, where the methacrylic acid (MAA) with its carboxylic groups was used again for the proton conductivity and divinylbenzene (DVB) to stabilise the polymers. The used initiator was again tert-butyl peroxide(TBPO). The structure of this materials is shown in figure 4.15.

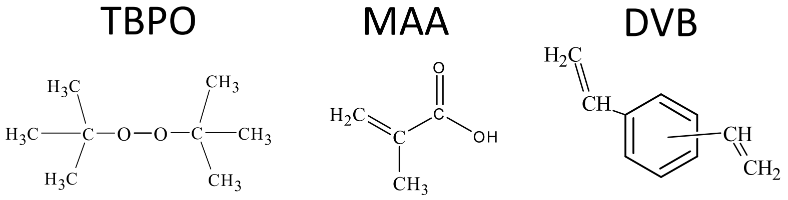

Figure 4.15: Chemical structure of TBPO, MAA and DVB.

DVB acts as crosslinker that connects the MAA polymer chains, to create a polymer network that should lead to a higher stability as shown in figure 4.16

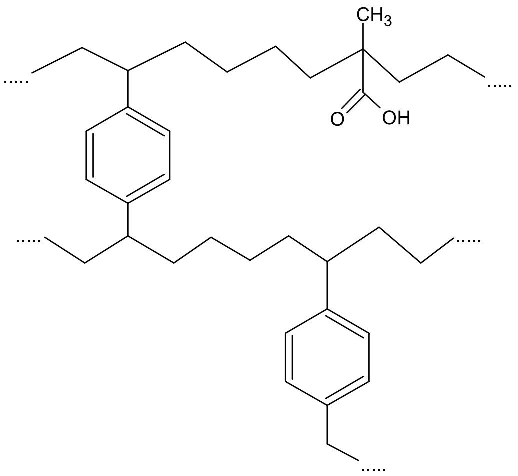

Figure 4.16: Schematic of a crosslinked MAA-DVB network.

The used flow rates and experimental parameters can be found in the experimental section for the MAA-DVB polymers in table 6.2. While the total flow rate for the deposition of the perfluorinated membranes was kept at $5.7\,sccm$ the total flow rate for the deposition of hydrocarbon membranes was kept at $3.0\,sccm$, to reach higher deposition rates. Since the reactivity of the DVB is lower compared to the very reactive PFDA, also a higher flow rate of this comonomer was used. The obtained deposition rates, the MAA fraction on the surface (f_{MAA}) as well as the MAA fraction in the copolymer (F_{MAA}) is summarized in table 4.3. The obtained deposition rates were ranging from 4.1 to $8.3\,nm/min$.

4.2.1 Chemical Composition

To determine the actual fraction of MAA in the polymer, the films were investigated by FTIR spectroscopy, which is shown in figure 4.17. The carbonyl group (COOH) showed a dominant absorption for $C=O$ stretch at $1706\,cm^{-1}$ and the absorbance increased, as the fraction of MAA in the copolymer increased. A broadband absorption of the $C-H$ stretch was observed between $3000\,cm^{-1}$ and $2750\,cm^{-1}$. In the lower frequency range from $1500\,cm^{-1}$ and $500\,cm^{-1}$ characteristic absorptions of the MAA and the DVB overlapped and where rather weak, therefore it was not possible to assign it to certain bond vibrations (see also table 3.1).

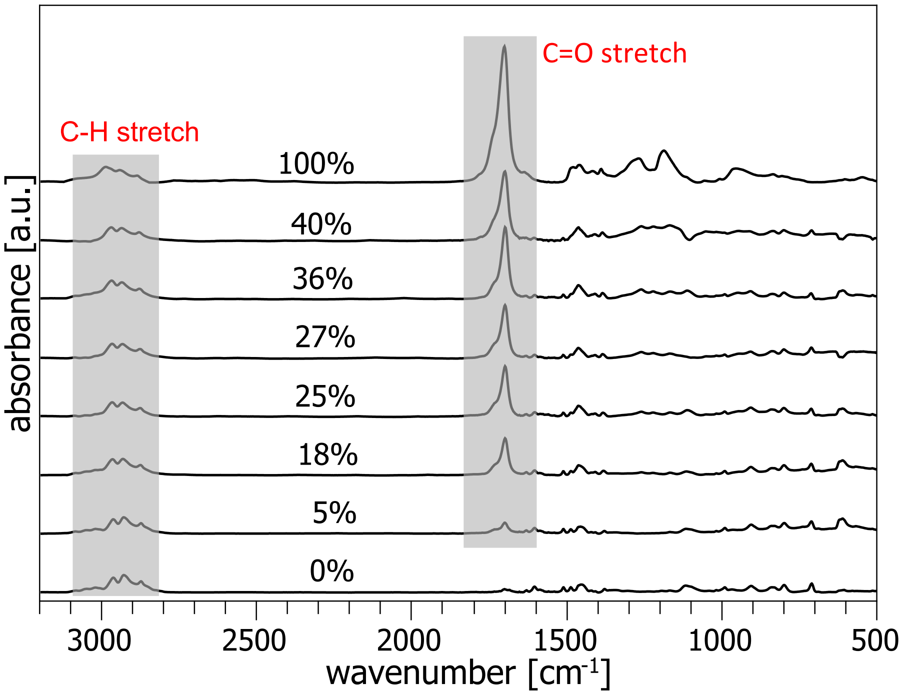

Figure 4.17: FTIR spectra of MAA-DVB polymer films. The labelled percentage is the fraction of MAA in the polymer.

The MAA fraction on the surface f_{MAA} was calculated from the P_M/P_{sat} ratio via (3.9). Since DVB has no COOR groups it was not possible to determine the MAA fraction in the polymer individually by a multiple Gauss fit as it was done for the MAA-PFDA copolymers. Instead, the MAA fraction in the copolymer (F_{MAA}), that is denoted in figure 4.17 was determined by calculating the fraction of the area under the $C = O$ peak of the copolymers at $1706\,cm^{-1}$ and the MAA homopolymer reference.

Table 4.3: Deposition rates and MAA fraction on the surface (f_{MAA}) and in the MAA-DVB copolymers (F_{MAA})

Sample	Dep. rate [nm/min]	f_{MAA} [%]	F_{MAA} [%]
A	4.1	0	0
B	5.8	7	5
C	5.8	13	18
D	5.8	19	25
E	7.1	24	27
F	6.9	28	36
G	5.2	44	40
H	8.3	100	100

The fraction of MAA in the copolymers as a function of MAA in the copolymers is plotted in figure 4.18. It shows an increasing trend of F_{MAA} versus f_{MAA}, which means, that as expected, the fraction of MAA in the copolymer increases as the MAA fraction at the surface increases.

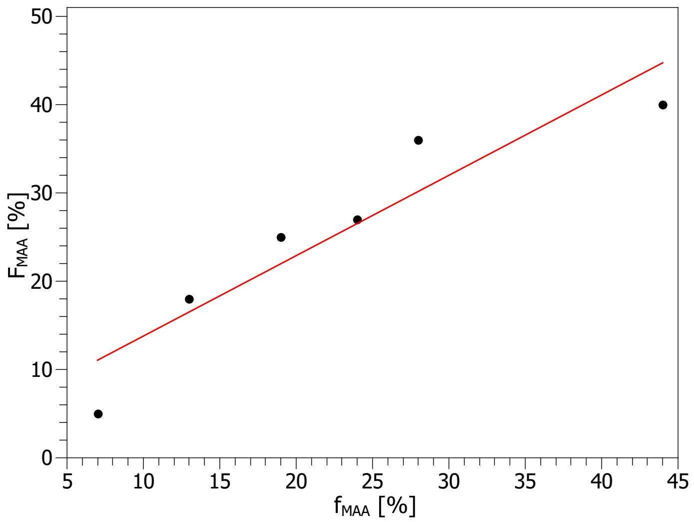

Figure 4.18: Plot of the fraction of MAA in the copolymers F_{MAA} versus the fraction of MAA at the surface f_{MAA}.

As already emphasized in previous sections, during operation the membrane needs to be immersed in water to reach high proton conductivities and therefore the membranes needs to be stable in water. Stability tests were performed in water for 24 hours at room temperature ($22°C$). The thickness of the films was measured with ellipsometry before and after the immersion and showed no significant change. It was also investigated if the immersion in water has an impact on the chemical composition and therefore FTIR measurements of the films were performed before and after the water treatment. In this particular test the films were immersed in water for $5\,h$ at room temperature and then dried at air for $24\,h$ before taking the second FTIR measurement.

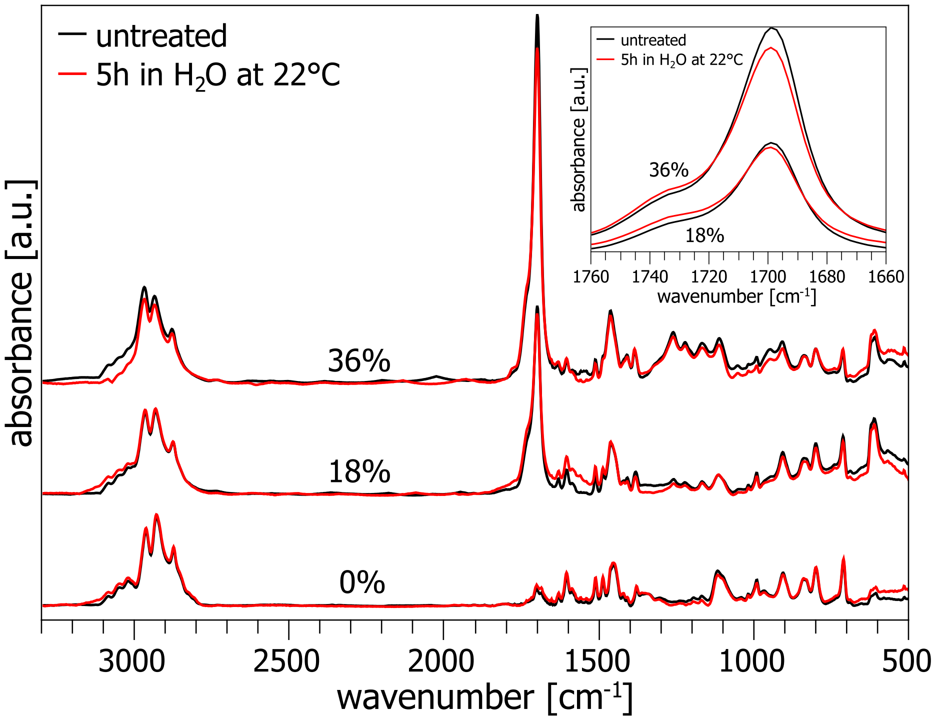

Figure 4.19: FTIR spectra of copolymer films before and after water treatment. The inset shows the change of the carbonyl peak that is caused by the water treatment. The labelled percentage is the fraction of MAA in the polymer.

Figure 4.19 shows the FTIR spectra before and after water treatment of the DVB homopolymer, and the copolymers with a MAA fraction of 18% and 36%, respectively. The spectra for the DVB homopolymer before and after water treatment matches and shows no significant difference, but for the copolymers some differences occurred. The $C-H$ stretch broadband between $2750cm^{-1}$ and $3000cm^{-1}$ showed some changes on the left-hand side shoulder. This was not a systematic change and can not be assigned to an underlying microscopic effect. The inset shows the more interesting $C=O$ stretch of the carbonyl group of the copolymers before and after soaking in water. While the absorbance at $1700\,cm^{-1}$ is reduced, it increased at the shoulder around $1735\,cm^{-1}$ after water treatment. This is probably caused by some rearrangement of the polymer chains due to the water treatment, which led a higher resonance frequency of the $C = O$ and therefore a shift of the peak to higher wavenumbers.

4.2.2 Crystallographic Investigation

Wide angle X-ray diffraction was measured for both the MAA and DVB homopolymer as well as a copolymer with 36% MAA fraction. It was expected to observe no crystalline structure since both, the MAA and the DVB are short molecules that can arrange easily in an amorphous state. The XRD measurements confirmed this expectations since no Bragg reflections were observed, as can be seen in figure 4.20.

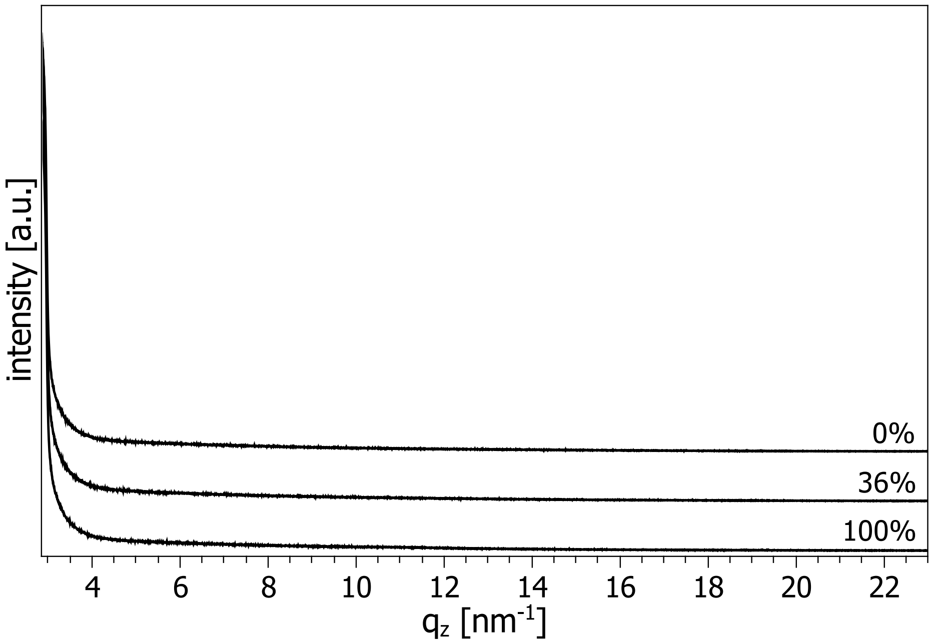

Figure 4.20: X-ray diffraction measurements of MAA-DVB polymers

4.2.3 Surface Morphology

The surface morphology was investigated with AFM in tapping mode. Figure 4.21 shows topographical images of the DVB homopolymer (a), a copolymer with 18% MAA fraction (b), a MAA homopolymer (c) as well as plot of the RMS roughness versus the MAA fraction (d). All films were very smooth and the RMS roughness showed no significant change.

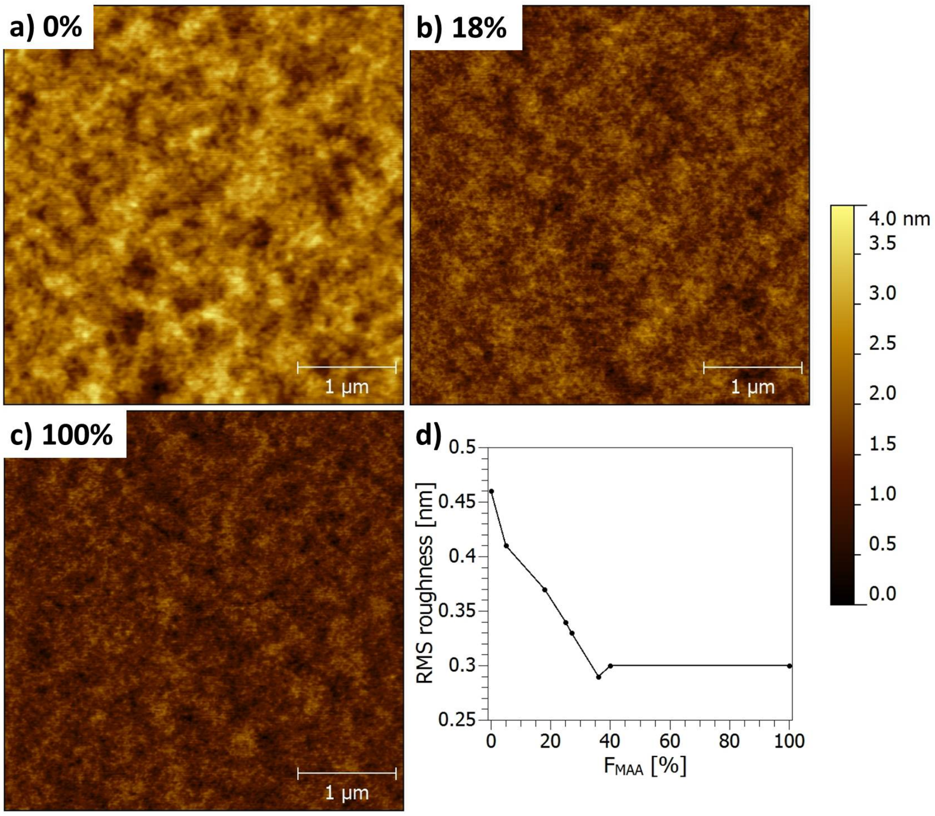

Figure 4.21: AFM investigation of MAA-DVB polymer films (a-c) and a plot of the RMS roughness of the polymer films which were deposited on a silicon wafer. The labelled percentage is the fraction of MAA in the polymer

4.2.4 Dynamic Water Contact Angle

To gain information about the chain mobility, advancing (WCA_{adv}) and receding (WCA_{rec}) water contact angles were measured on the copolymer films and on the DVB homopolymer (see figure 4.22). Again it was not possible to measure the water contact angle on the MAA homopolymer since it dissolved during the measurement.

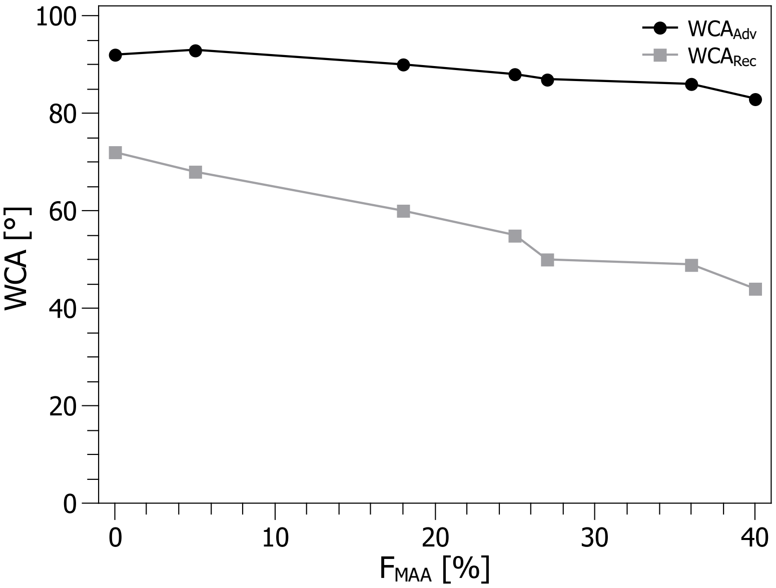

Figure 4.22: Dynamic water contact angle measurement of MAA-DVB polymers

The polymers were rather hydrophilic. The advancing water contact angle showed only a slight change for the different compositions and was in the range between $83°$ and $93°$, showing a trend to lower contact angles for polymers with higher MAA fraction. The receding water contact angle showed a steady decrease with the MAA fraction from $72°$ to $44°$, which led to an increase in the hysteresis from $20°$ to $39°$. Since it was shown that MAA-DVB polymers were amorphous, an effect of crystallinity that causes the change in the hysteresis can be excluded. Also the surface morphology investigation with AFM showed that there is no influence from the surface roughness. Therefore, this increase in the hysteresis is probably caused by the reduction of the DVB units and thus the crosslinking of the polymer chains for high MAA fractions. Therefore the hydrophilic groups of the MAA can more easily re-orient to be exposed in the water drop.

4.2.5 PTFE Carrier

To measure the proton conductivity with impedance spectroscopy, the polymers were deposited again on a PTFE carrier. Since PTFE is hydrophobic it was investigated if hydrophilic MAA-DVB polymers can conformally coat this film.

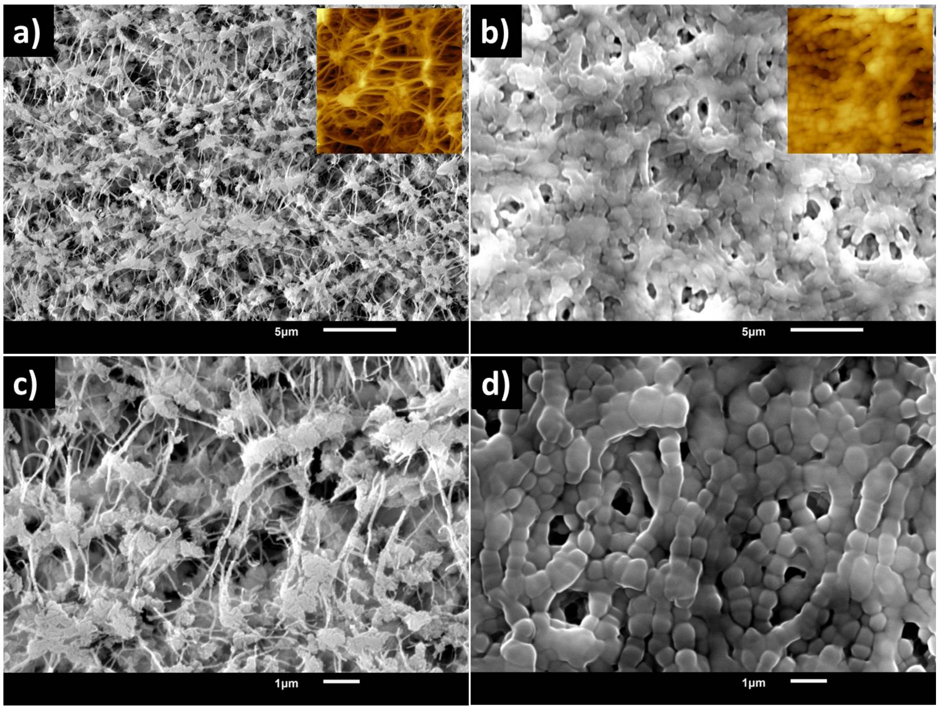

Figure 4.23: SEM and AFM investigation of an uncoated PTFE film (a,c) and coated with $1\mu m$ MAA-DVB copolymer with 36% MAA fraction (b,d), at different magnifications

The structure of PTFE film consists of PTFE knots that are connected by thin wires, which can bee seen in figure 4.23a and 4.23c. This structure was more or less conformally coated by the MAA-DVB copolymer, although it can be observed that the coated wires look more like a caterpillar rather than tubes. This could either be caused by the complexity of the PTFE film structure or by the chemical heterogeneity between the film and the polymer coating. The thickness of the coating was monitored during the deposition by Laser interferometry on a silicon wafer and was approximately $1\,\mu m$. On the PTFE carrier this coating seems to be significantly thinner. Differences in the temperature on silicon wafer and on the PTFE carrier surface, could have led to this discrepancy, since the substrate temperature impacts the adsorption of the monomers on the surface and therefore the deposition kinetics. The coating did not completely close the pores and flatten the surface since the pores evidently appear bigger than their nominal size of $0.45\,\mu m$, but the pores were reduced and the surface was flattened to some extent.

4.2.6 Proton Conductivity

The proton conductivity of hydrocarbon membranes which was reported in literature extends over orders of magnitude, depending on the used chemistry, from conductivities comparable to Nafion® to conductivities that are orders of magnitude lower. [2] Therefore, a low proton conductivity was expected for the MAA-DVB copolymers. The measurement of the proton conductivities of the MAA-DVB polymers faced the same difficulties as described in section 4.1.5. Again, due to the low film thickness of $1\,\mu m$, the measured resistance was high and for the MAA-DVB copolymers, the measured resistance of the blank water and the water with the immersed membrane was approximately the same. This indicates a very low proton conductivity, probably orders of magnitude lower than Nafion®, which was not measurable on the $1\,\mu m$ film with the used setup. Although the water contact angle hysteresis was high and increased with the MAA fraction, it showed no impact on the measured membrane resistance.

5 Conclusions

5.1 MAA-PFDA Polymers

Proton conductive polymers of MAA and PFDA were synthesized and their microscopical structure was investigated. The copolymers were stable below a MAA fraction of $50\,\%$. Both the homopolymer and the copolymer showed an out-of-plane order, which disappeared with increasing MAA fraction. The net plane distance of the out-of-plane order was increased by the presence of MAA units from $3.19\,nm$ for the PFDA homopolymer to $3.56\,nm$ for the MAA-PFDA copolymer with $41\,\%$ MAA. This proofed that it is indeed a crystalline copolymer structure and not a phase separation between the crystalline PFDA and the amorphous MAA. Out of this, a hypothetical model for the MAA-PFDA bilayer structure was proposed. It was also shown that the hexagonal in-plane order of the PFDA homopolymer gets lost for the MAA-PFDA copolymer. X-ray diffraction measurements at different tilt angles demonstrated that the chains of the homopolymer and the copolymer have a preferred orientation at 0°. Together with the out-of-plane organization of the chains it can be concluded that the MAA-PFDA copolymer crystallizes into a smectic A phase, while the PFDA homopolymer with its additional hexagonal in-plane order crystallizes into a smectic B phase. Dynamic water contact angle measurements revealed, that the polymer chains have a high mobility, which can be beneficial for the proton conductivity. Electrochemical impedance spectroscopy proofed that the MAA-PFDA copolymers are capable of transporting protons and showed very promising conductivities for the copolymers with high MAA fraction and obtained a maximum of $55\,mS/cm$ for the copolymer with 41% MAA fraction. Therefore this copolymers are an interesting and cheap alternative to Nafion®.

5.2 MAA-DVB Polymers

In the second approach proton conductive polymers were synthesized out of the hydrocarbon monomers methacrylic acid (MAA) and divinylbenzene (DVB). This copolymers were also stable in water below $50\,\%$ MAA fraction. The copolymers were in an amorphous phase and showed no organization in planes. The high hysteresis between the advancing and receding contact angle increased with the MAA fraction from $20°$ for the DVB homopolymer to $39°$ for the copolymer with 40% MAA. From the crystallographic and morphological investigations it was concluded that the high hysteresis from the homopolymer is caused by the amorphous film, but the increase in the hysteresis for the copolymers is due to an increasing chain mobility. Although the the water contact angle measurements indicated a high chain mobility, the proton conductivity was too low to measure on the $1\,\mu m$ films with the used setup, but was probably orders of magnitude lower than the conductivity of Nafion® and of the MAA-PFDA copolymers, respectively. Therefore this copolymers are no suitable candidate for the use as proton exchange membranes.

6 Appendix

6.1 Experimental MAA-PFDA Copolymers

MAA-PFDA polymers were polymerized by initiated chemical vapor deposition (iCVD) on silicon substrates (Siegert Wafer), with a desired film thickness around $100\,nm$. Additionally, approximately $1\,\mu m$ thick films were deposited on a porous PTFE carrier film (Goodfellow), with a thickness of $63\,\mu m$, a porosity of 84% and a pore size of $0.45\,\mu m$ for the proton conductivity measurements.

6.1.1 Materials

The hydrophilic monomer (methacrylic acid, MAA, $99\,\%$, Aldrich), the hydrophobic comonomer (1H, 1H, 2H, 2H, -perflourodecyl acrylate, PFDA, $97\,\%$, Aldrich) and the initiator (tert-butyl peroxide, TBPO, $98\,\%$ Aldrich) were used without any further purification.

6.1.2 Experimental Setup

The depositions were made in a custom-built cylindrical vacuum reactor with a diameter of $36\,cm$ and a height of $5.5\,cm$, which is shown in figure 6.1. The top of the reactor was a removable $2.5\,cm$ thick quartz blade which allowed to monitor the film thickness with Laser interferometry, with a He-Ne Laser (Thorlabs, $\lambda = 633\,nm$). To evacuate the chamber a rotary pump (Pfeifer Duo 5M) was used and the pressure was monitored with a MicroPirani Gauge (Balzers). The pressure was kept at $800\,mTorr$ during the depositions. While the initiator vaporizes already at room temperature, the MAA needed to be heated up to $70°C$ and the PFDA to $80°C$, respectively. To control the flow rates of the monomers and the initiator, needle valves (Swagelok) were used. The Nitrogen flow rate was controlled with a Mass Flow Controller (MKS). To create radicals the labile peroxide bond of the initiator was thermally broken by a filament array, which consisted of 12 parallel nickel-chromium wires (Goodfellow), $2.5\,cm$ above the substrate. The filaments were heated up to $(284 \pm 3)°C$ with a DC power supply (Heinzinger PTN 350-5). The substrate temperature was controlled with a chiller/heater (Thermo Scientific Accel 500 LC) to $(50 \pm 5)°C$. All temperatures were monitored by type K thermocouples (Omega Engineering). The experiments were carried out with a constant initiator flow rate of $(1.00 \pm 0.05)\,sccm$ and a constant PFDA flow rate of $(0.30 \pm 0.03)\,sccm$ while the MAA and Nitrogen flow rate was adjusted to keep the total flow rate at $5.7\,sccm$. The flow rates are summarized in table 6.1. This depositions were repeated with a higher film thickness ($200\,nm$) and with a higher substrate temperature ($60°C$) for a film thickness of $100\,nm$ and $200\,nm$. All series showed very similar results and the reported results are from the series with a film thickness of $100\,nm$ and a substrate temperature of $50°C$.

Table 6.1: Flow rates used for the growth of MAA-PFDA copolymers by iCVD

Sample	MAA flow rate $[sccm]$	PFDA flow rate $[sccm]$	TBPO flow rate $[sccm]$	N_2 flow rate $[sccm]$	P_M/P_{sat} MAA	P_M/P_{sat} PFDA
A	0.0	0.3	1.0	4.4		0.126
B	0.3	0.3	1.0	4.1	0.006	0.126
C	0.6	0.3	1.0	3.8	0.013	0.126
D	1.0	0.3	1.0	3.4	0.021	0.126
E	1.4	0.3	1.0	3.0	0.030	0.126
F	3.0	0.0	1.0	1.7	0.064	

6.1.3 Characterization

The thickness of the deposited films, which was monitored by Laser interferometry was measured ex situ by ellipsometry (VASE, M-2000, J.A. Woolam) and was $130 \pm 15\,nm$. The chemical composition and structure of the films were investigated by Fourier transform infrared (FTIR) spectroscopy (Brucker IFS 66v/S). The measurements were carried out in transmission mode. The spectra were recorded from 4000 to $400\,cm^{-1}$ at a resolution of $4\,cm^{-1}$ and were averaged over 100 scans to improve the signal-to-noise ratio. All spectra were manually baseline-corrected. A non-linear least-squares regression was performed on the absorption peak at $1690 - 1760\,cm^{-1}$ using two Gaussian components with the "Multiple Gauss Peaks" procedure of the qti-Plot software. To investigate the structure of the films, various X-ray based techniques were used. To observe Bragg peaks and thus conclude the crystalline structure, the films were investigated by standard X-ray diffraction (XRD) $\theta - 2\theta$ scans (Philips PW1830, $\lambda = 2.28975\,\text{Å}$) and by $\theta - 2\theta$ scans within the reflectivity regime (X-ray reflectivity - XRR) (Empyrian Panalytical, $\lambda = 1.54178\,\text{Å}$). Grazing incidence X-ray diffraction (GIXD) measurements on a series of samples were carried out using the synchrotron facility BESSY, beamline KMC2. The film morphology and the surface roughness were investigated with an atomic force microscope (Veeco Dimension 3100) in tapping mode. Advancing and receding water contact angles (WCA) were measured in dynamic mode by Rame-Hart 200 goniometer, with sessile drop method. The contact angles were measured by depositing a $2\,\mu l$ droplet on the surface then increasing it in steps of $0.25\,\mu l$ to $4\,\mu l$, finally decreasing it in steps of $0.25\,\mu l$ until the receding was observed. Advancing angles were considered as the maximum observed angle just before the droplet advanced. Receding contact angles were measured in correspondence of the drop profile just before the contact surface reduction. Each WCA value was averaged from measurements of eight drops with an estimated maximum error of $6\,\%$. The in-plane proton conductivity was measured with electrochemical impedance spectroscopy (Gamry Instruments, Reference 600) with a 4 point probe. An alternating voltage signal of RMS $50\,mV$ was applied in the frequency range from $0.1 - 10000\,Hz$ and 5 points per decade were recorded. The open circuit voltage was measured for $50\,s$ before the measurements to adjust the working point. The measurements were carried out at room temperature in approximately $400\,ml$ of ultra pure water ($17.4\,M\Omega\,cm$). The distance between the inner voltage-sensing electrodes was $0.425\,cm$. The samples were cut into stripes with a width between $1.1\,cm$ and $1.4\,cm$ and were mounted in a BT-110 Conductivity Clamp (Scribner Associates).

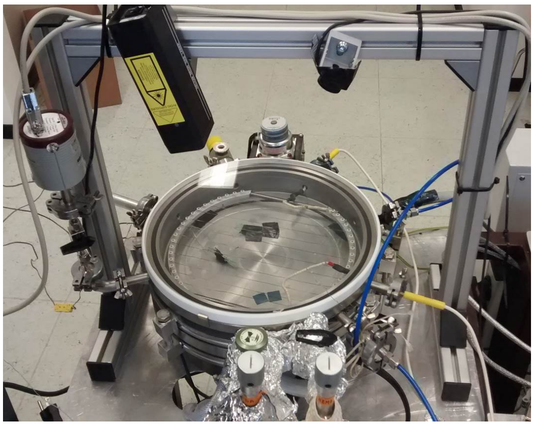

Figure 6.1: iCVD reactor that was used to synthesize MAA-PFDA polymers

6.2 Experimental MAA-DVB Copolymers

MAA-DVB polymers were polymerized by initiated chemical vapor deposition (iCVD) on silicon substrates (Wafer World), with a desired film thickness around $1 \mu m$. This films were deposited simultaneously on a porous PTFE carrier film (Goodfellow), with a thickness of $63\,\mu m$, a porosity of 84% and a pore size of $0.45\,\mu m$ for the proton conductivity measurements.

6.2.1 Materials

The hydrophilic monomer (methacrylic acid, MAA, $99\,\%$, Aldrich), the crosslinker (Divinylbenzene, DVB, 80 Aldrich) and the initiator (tert-butyl peroxide, TBPO, $98\,\%$ Aldrich) were used without any further purification.

6.2.2 Experimental Setup

The depositions were made in a custom-built cylindrical vacuum reactor with a diameter of $25\,cm$ and a height of $3.8\,cm$, which is shown in figure 6.2. The top of the reactor was a removable quartz blade which allowed to monitor the film thickness with Laser interferometry, with a He-Ne Laser (JDS Uniphase, $\lambda = 633\,nm$). To evacuate the chamber a rotary pump (Marathon Electric) was used and the pressure was monitored with a capacitance manometer (MKS Instruments, MKS 622). The pressure during the depositions was kept at $500\,mTorr$ using a throttle valve (MKS instruments). While the initiator vaporizes already at room temperature, the MAA needed to be heated up to $60°C$ and the DVB to $40°C$, respectively with heating tapes (Omega Engineering) and a custom built controller. To control the flow rates of the monomers, needle valves (Swagelok) were used. The Nitrogen flow rate as well as the initiator flow rate was controlled with mass flow controller (MKS). To create radicals the labile peroxide bond of the initiator was thermally broken by a filament array (Goodfellow), which consisted of 14 parallel chrome alloy filaments, $1.5\,cm$ above the substrate. The filaments were heated up to $(280 \pm 5)°C$ with a DC power supply (Sorensen DHP Series). The substrate temperature was controlled with a chiller/heater (Neslab RTE 7) to $(30 \pm 5)°C$. All temperatures were monitored by type K thermocouples (Omega Engineering). The experiments were carried out with a constant initiator flow rate of $(1.00 \pm 0.05)\,sccm$, while the MAA, DVB and Nitrogen flow rate was adjusted to vary the ratio of carboxylic groups. The

Table 6.2: Flow rates used for the growth of MAA-DVB copolymers by iCVD

Sample	MAA flow rate $[sccm]$	DVB flow rate $[sccm]$	TBPO flow rate $[sccm]$	N_2 flow rate $[sccm]$	P_M/P_{sat} MAA	P_M/P_{sat} PFDA
A	0.0	1.0	1.0	1.0		0.222
B	0.2	1.0	1.0	0.8	0.017	0.222
C	0.4	1.0	1.0	0.6	0.034	0.222
D	0.6	1.0	1.0	0.4	0.051	0.222
E	0.8	1.0	1.0	0.2	0.068	0.222
F	1.0	1.0	1.0	0.0	0.086	0.222
G	1.0	0.5	1.0	0.5	0.086	0.111
H	2.0	0.0	1.0	0.0	0.171	

total flow rate was kept at $3.0\,sccm$. The used flow rates are summarized in table 6.2.

6.2.3 Characterization

The thickness of the deposited films, which was monitored by Laser interferometry was measured ex situ by ellipsometry (VASE, M-2000, J.A. Woolam) and was $1000 \pm 50\,nm$. The chemical composition and structure of the films was investigated by Fourier transform infrared (FTIR) spectroscopy (Nicolet iS50). The measurements were carried out in transmission mode. The spectra were recorded from 4000 to $400\,cm^{-1}$ at a resolution of $4\,cm^{-1}$. To investigate the structure of the polymers, the films were investigated by standard X-ray Diffraction (XRD) $\theta - 2\theta$ scans (Empyrian Panalytical, $\lambda = 1.54178\,\text{Å}$). The film morphology and the surface roughness were investigated with an atomic force microscope (Veeco Dimension 3100) in tapping mode. The structure of an uncoated and coated PTFE carrier film was investigated by AFM in tapping mode and by scanning electron microscopy (JEOL JSM-6010LA). To avoid charging effects the samples were coated with a approximately $6\,nm$ thick gold film. Advancing and receding water contact angles (WCA) were measured in dynamic mode by Rame-Hart 200 goniometer, with sessile drop method. The contact angles were measured by depositing a $2\,\mu l$ droplet on the surface then increasing it in steps of $0.25\,\mu l$ to $4\,\mu l$, finally decreasing it in steps of $0.25\,\mu l$ until the receding was observed. Advancing angles were considered as the maximum observed angle just before the droplet advanced. Receding contact angles were measured in correspondence of the drop profile just before the contact surface reduction. Each WCA value was averaged from measurements of four drops with an estimated maximum error of $2\,\%$ for the advancing and $9\,\%$ for the receding contact angle. The in-plane proton conductivity was measured with electrochemical impedance spectroscopy (Gamry Instruments, Reference 600) with a 4 point probe. An alternating voltage signal of RMS $50\,mV$ was applied in the frequency range from $0.1 - 10000\,Hz$ and 5 points per decade were recorded. The open circuit voltage was measured for $50\,s$ before the measurements to adjust the working point. The measurements were carried out at room temperature in approximately $400\,ml$ of ultra pure water ($17.4\,M\Omega\,cm$). The distance between the inner voltage-sensing electrodes was $0.425\,cm$. The samples were cut into stripes with a width between $1.1\,cm$ and $1.4\,cm$ and were mounted in a BT-110 Conductivity Clamp (Scribner Associates).

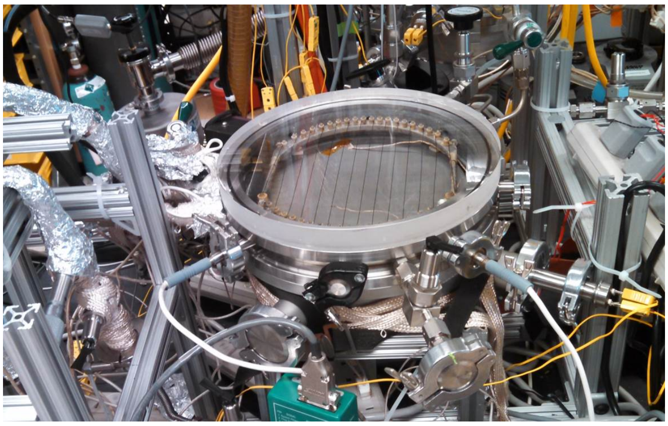

Figure 6.2: iCVD reactor that was used to synthesize MAA-DVB polymers

Bibliography

[1] Y. Wang, K. S. Chen, J. Mishler, S. C. Cho, and X. C. Adroher, "A review of polymer electrolyte membrane fuel cells: technology, applications, and needs on fundamental research," *Applied Energy*, vol. 88, no. 4, pp. 981–1007, 2011.

[2] M. Rikukawa and K. Sanui, "Proton-conducting polymer electrolyte membranes based on hydrocarbon polymers," *Progress in Polymer Science*, vol. 25, no. 10, pp. 1463–1502, 2000.

[3] A. Sahu, S. Pitchumani, P. Sridhar, and A. Shukla, "Nafion and modified-Nafion membranes for polymer electrolyte fuel cells: An overview," *Bulletin of Materials Science*, vol. 32, no. 3, pp. 285–294, 2009.

[4] S. Bhatt, B. Gupta, V. Sethi, and M. Pandey, "Polymer exchange membrane (PEM) fuel cell: A review," *International Journal of Current Engineering and Technology*, vol. 2, no. 1, 2012.

[5] B. Smitha, S. Sridhar, and A. Khan, "Solid polymer electrolyte membranes for fuel cell applications-a review," *Journal of Membrane Science*, vol. 259, no. 1, pp. 10–26, 2005.

[6] W. Y. Hsu and T. D. Gierke, "Ion transport and clustering in Nafion perfluorinated membranes," *Journal of Membrane Science*, vol. 13, no. 3, pp. 307–326, 1983.

[7] K. A. Mauritz and R. B. Moore, "State of understanding of Nafion," *Chemical reviews*, vol. 104, no. 10, pp. 4535–4586, 2004.

[8] J. Peron, Z. Shi, and S. Holdcroft, "Hydrocarbon proton conducting polymers for fuel cell catalyst layers," *Energy & Environmental Science*, vol. 4, no. 5, pp. 1575–1591, 2011.

[9] A. Rudin and P. Choi, *The Elements of Polymer Science & Engineering*. Academic Press, 2012.

[10] P. Atkins, *Physical chemistry*. Oxford University Press, 1994.

[11] A. M. Coclite, R. M. Howden, D. C. Borrelli, C. D. Petruczok, R. Yang, J. L. Yagüe, A. Ugur, N. Chen, S. Lee, W. J. Jo, *et al.*, "25th anniversary article: CVD polymers: A new paradigm for surface modification and device fabrication," *Advanced Materials*, vol. 25, no. 38, pp. 5392–5423, 2013.

[12] A. M. Coclite, P. Lund, R. Di Mundo, and F. Palumbo, "Novel hybrid fluoro-carboxylated copolymers deposited by initiated chemical vapor deposition as protonic membranes," *Polymer*, vol. 54, no. 1, pp. 24–30, 2013.

[13] S. Chandrasekhar, *Liquid crystals*. Cambridge University Press, 1977.

[14] J. Garcia-Amorós and D. Velasco, "Polysiloxane side-chain azobenzene-containing liquid single crystal elastomers for photo-active artificial muscle-like actuators," 2012.

[15] H. Gao and K. Lian, "Proton-conducting polymer electrolytes and their applications in solid supercapacitors: a review," *RSC Advances*, vol. 4, no. 62, pp. 33091–33113, 2014.

[16] J. Zhang, J. Wu, and H. Zhang, *PEM fuel cell testing and diagnosis*. Newnes, 2013.

[17] K.-D. Kreuer, S. J. Paddison, E. Spohr, and M. Schuster, "Transport in proton conductors for fuel-cell applications: simulations, elementary reactions, and phenomenology," *Chemical Reviews*, vol. 104, no. 10, pp. 4637–4678, 2004.

[18] M. Birkholz, *Thin film analysis by X-ray scattering*. John Wiley & Sons, 2006.

[19] K. K. Lau and K. K. Gleason, "Initiated chemical vapor deposition (iCVD) of poly (alkyl acrylates): an experimental study," *Macromolecules*, vol. 39, no. 10, pp. 3688–3694, 2006.

[20] H. Yasuda, *Plasma polymerization*. Academic press, 1985.

[21] K. K. Lau and K. K. Gleason, "Initiated chemical vapor deposition (iCVD) of poly (alkyl acrylates): A kinetic model," *Macromolecules*, vol. 39, no. 10, pp. 3695–3703, 2006.

[22] B. Reeja-Jayan, P. Kovacik, R. Yang, H. Sojoudi, A. Ugur, D. H. Kim, C. D. Petruczok, X. Wang, A. Liu, and K. K. Gleason, "A route towards sustainability through engineered polymeric interfaces," *Advanced Materials Interfaces*, 2014.

[23] P. Larkin, *Infrared and Raman spectroscopy; principles and spectral interpretation*. Elsevier, 2011.

[24] P. R. Griffiths and J. A. De Haseth, *Fourier transform infrared spectrometry*, vol. 83. John Wiley & Sons, 1986.

[25] Panalytical, “Heavy mineral sand analysis for industrial process control,” tech. rep., http://www.azomining.com/article.aspx?ArticleID=160 (visited on October 25, 2014).

[26] C. Wei, H. Pang, B. Zhang, Q. Lu, S. Liang, and F. Gao, “Two-dimensional [bgr]-MnO2 nanowire network with enhanced electrochemical capacitance,” *Scientific reports*, vol. 3, 2013.

[27] P. Scherrer, “Bestimmung der Gröesse und der inneren Struktur von Kolloidteilchen mittels Röntgenstrahlen,” *Nachrichten von der Gesellschaft der Wissenschaften zu Göttingen, Mathematisch-Physikalische Klasse*, vol. 1918, pp. 98–100, 1918.

[28] A. Patterson, “The Scherrer formula for X-ray particle size determination,” *Physical review*, vol. 56, no. 10, p. 978, 1939.

[29] O. Werzer, B. Stadlober, A. Haase, M. Oehzelt, and R. Resel, “Full X-ray pattern analysis of vacuum deposited pentacene thin films,” *The European Physical Journal B-Condensed Matter and Complex Systems*, vol. 66, no. 4, pp. 455–459, 2008.

[30] M. Neuschitzer, A. Moser, A. Neuhold, J. Kraxner, B. Stadlober, M. Oehzelt, I. Salzmann, R. Resel, and J. Novak, “Grazing-incidence in-plane X-ray diffraction on ultra-thin organic films using standard laboratory equipment,” *Journal of Applied Crystallography*, vol. 45, no. 2, pp. 367–370, 2012.

[31] R. Förch, H. Schönherr, and A. T. A. Jenkins, *Surface design: applications in bioscience and nanotechnology*. John Wiley & Sons, 2009.

[32] R. Di Mundo and F. Palumbo, “Comments regarding "an essay on contact angle measurements",” *Plasma Processes and Polymers*, vol. 8, no. 1, pp. 14–18, 2011.

[33] K. Honda, M. Morita, H. Otsuka, and A. Takahara, “Molecular aggregation structure and surface properties of poly (fluoroalkyl acrylate) thin films,” *Macromolecules*, vol. 38, no. 13, pp. 5699–5705, 2005.

[34] W. R. Bowen and N. Hilal, *Atomic Force Microscopy in Process Engineering: An Introduction to AFM for Improved Processes and Products*. Butterworth-Heinemann, 2009.

[35] N. A. Geisse, "AFM and combined optical techniques," *Materials today*, vol. 12, no. 7, pp. 40–45, 2009.

[36] J. Goldstein, D. E. Newbury, D. Joy, and C. Lyman, "Scanning electron microscopy and X-ray microanalysis. 2003," *ISBN*, vol. 306472929, p. 9780306472923.

[37] E. Dedmond and K. Cooper, "Application note - effect of solution conductivity on in-plane membrane conductivity measurement," tech. rep., Scribner Associates, Inc.

[38] C. Ranacher, R. Resel, P. Moni, S. Weinberger, B. Cermenek, V. Hacker, and A. M. Coclite, "Layered nanostructures in proton conductive polymers obtained by initiated chemical vapor deposition," *UNDER REVISION*, 2015.

[39] A. M. Coclite, Y. Shi, and K. K. Gleason, "Controlling the degree of crystallinity and preferred crystallographic orientation in poly-perfluorodecylacrylate thin films by initiated chemical vapor deposition," *Advanced Functional Materials*, vol. 22, no. 10, pp. 2167–2176, 2012.

[40] J. L. Yagüe and K. K. Gleason, "Enhanced cross-linked density by annealing on fluorinated polymers synthesized via initiated chemical vapor deposition to prevent surface reconstruction," *Macromolecules*, vol. 46, no. 16, pp. 6548–6554, 2013.